Track structure of light ions: experiments and simulations

2012 New J. Phys. 14 093010

(http://iopscience.iop.org/1367-2630/14/9/093010)

New Journal of Physics
The open-access journal for physics

Track structure of light ions: experiments and simulations

V Conte[1,4], P Colautti[1], B Grosswendt[2], D Moro[3] and L De Nardo[3]

[1] LNL-INFN, viale dell'Università 2, I-35020 Legnaro, Italy
[2] Austrian Institute of Technology, AIT, A-1220 Vienna, Austria
[3] PD-INFN and Physics and Astronomy Department of Padova University, via Marzolo 8, I-35100 Padova, Italy
E-mail: conte@lnl.infn.it

New Journal of Physics **14** (2012) 093010 (38pp)
Received 18 May 2012
Published 7 September 2012
Online at http://www.njp.org/
doi:10.1088/1367-2630/14/9/093010

Abstract. To study the track structure of light ions, a measuring device has been developed at the Legnaro National Laboratory of INFN, which can be used to investigate separately the penumbra region of particle tracks and the track-core region, which is a few nanometres in diameter. The device is based on single-electron counting techniques by means of a gas detector; it simulates a 'nanometre-sized' biological volume of about 20 nm in diameter that can be moved with respect to a narrow particle beam to measure the ionization-cluster-size distributions caused within the target volume by the passage of single primary particles, as a function of the impact parameter. To investigate the ionization-cluster-size formation caused by primary particles of medical interest when they penetrate through or pass by the target volume at a specified impact parameter, measurements and Monte Carlo simulations were performed for 20 MeV protons, 16 MeV deuterons, 48 MeV ^{6}Li-ions, 26.7 MeV ^{7}Li-ions and 96 MeV ^{12}C-ions. The detailed analysis of the resulting distributions showed that in the track-core region their shape is mainly determined by the mean free ionization path length of the primary particles, whereas in the penumbra region the shape of the distributions is almost independent of the impact parameter, and also of the particle type and velocity.

[4] Author to whom any correspondence should be addressed.

Contents

1. Introduction

The interaction of ionizing radiation with living cells can seriously affect their normal functionality, depending on whether a severe interaction occurs in a critical part of the cell, inducing a variety of biological effects such as loss of reproductive capacity, cancer or mutations leading to cell death. Hence, the knowledge of the biological effectiveness of ionizing radiation to reach particular radiobiological endpoints is of great importance, particularly in the fields of treatment planning for ion therapy (Elsässer *et al* 2008, Kase *et al* 2008), and of radiation protection, for instance, for risk assessment in space (see Cucinotta and Durante 2006).

At present, radiation therapy is performed for the greater part with high-energy photons, but hadron therapy is an emerging treatment modality, especially for certain radioresistant cancers and for cancerous *tumours close to critical organs*. The twofold advantage of hadron therapy with respect to conventional radiotherapy is related (i) to higher radiobiological effectiveness, and (ii) to higher precision dose delivering. Currently, there are 25 clinical facilities for proton therapy worldwide in operation, while six facilities provide carbon-ion treatment, and many others are in the planning stage or under construction. Starting from the seventies, about 70 000 patients have been treated, with encouraging results. An overview of light-ion beam therapy can be found in the literature (for instance, Chu 2007, Amaldi and Kraft 2007).

As compared with photon therapy, the ionization density caused in light-ion therapy is markedly greater, in particular, at the end of the ranges of protons or heavier ions due to the track structure of low-energy ions. This track structure includes a high fraction of ionization processes within distances of a few nanometres and, thus, favours the formation of severe damage to sub-cellular targets (segments of the DNA, nucleosomes and segments of the chromosome fibre) the critical sizes of which are between about 3 and 30 nm.

The strong influence of track structure on the therapeutic effectiveness of ionizing radiation leads, however, to difficulties in radiation-treatment planning, which is used to determine the

dose distribution to be applied to the tumour volume during radiation therapy, in particular, for the purposes of radiation therapy using light ions. Conventionally, the quantity of the absorbed dose to water is applied for this purpose, despite the fact that it takes into account neither the stochastics of particle interaction in nanometre-sized volumes nor the track structure of ionizing particles. Because of this weakness, the absorbed dose can only be used to quantify the amount of energy transferred to matter but never also to quantify the radiation quality, which is decisive for the effectiveness of ionizing radiation to initiate radiation damage (Grosswendt 2007). In consequence, to improve treatment planning and, for instance, also risk assessment in space, the absorbed dose must be supplemented by the radiation quality applied in radiation therapy and by the corresponding radiobiological effectiveness, which should also be monitored by measurements during radiation therapy for purposes of quality assurance (Wambersie *et al* 2006).

Generally speaking, it can be assumed that the responses of cells to ionizing radiation are due to some rare events like the formation of double-strand breaks in the DNA, which result mainly from a clustering of initial damage (Goodhead 1994). The degree of this clustering is responsible for the complexity of the damage and is, of course, a result of the particle track structure, which is defined as the spatial distribution of inelastic particle interactions, supplemented by the atomic or molecular species formed at each interaction point by an ionizing particle during its penetration through matter. In this sense, it is obvious that the complexity of the damage increases if the distance between the points of the particle interactions decreases, with the result that the ability of cells to recognize and to repair correctly the damage clusters also decreases. The key for a general understanding of cellular responses is, therefore, the track structure of ionizing radiation, which depends on the target medium and on the radiation quality of ionizing radiation (particle type and particle velocity). In consequence, the measurement of track-structure properties independent of radiation quality and the characterization of these properties from the biophysical point of view are of the utmost importance.

As far as the measurements of track structure (the spatial distribution of the points of inelastic particle interactions) and of its potential influence on radiobiological effects are concerned, detectors are necessary that are comparable in size to the critical radiosensitive sub-structures of cell nuclei, at least in principle, and are able to be used to investigate separately the structure of a particle track in the so-called track-core region, and in the so-called penumbra region. This latter region is exclusively formed by the interactions of so-called δ-electrons, which are secondary electrons set in motion by ionization processes of the primary particles.

The most promising methods for such track-structure measurements are currently based on positive ion counting (Pszona *et al* 2000, Shchemelinin *et al* 2002, Bashkirov *et al* 2006, 2009) or low-energy electron counting techniques (De Nardo *et al* 2002a), and provide radiation-induced ionization-cluster-size distributions in nanometre-equivalent gas models of condensed matter (see Grosswendt 2006, Schulte 2011), which give a picture of the stochastics of particle interactions in nanometre-sized target volumes.

The measuring device, based on the single-electron counting technique, installed at the Legnaro National Laboratories of INFN, can be readily applied to study the track-core region of particle tracks and the penumbra region separately. It simulates a target volume of about 20 nm in diameter that can be moved with respect to a narrow primary particle beam, allowing the measurement of the ionization-cluster-size distribution mainly representing the track-core region of a particle track, and also of that describing the penumbra region,

as a function of the impact parameter with respect to the primary ion trajectory (De Nardo *et al* 2002a, 2007, Conte *et al* 2011).

Because of the importance of track-structure properties of ionizing particles for radiobiology and health physics, it is the aim of this work to investigate the formation of ionization-cluster-size distributions caused in a nanometre-sized volume by light ions when penetrating through or passing by the target volume at a specified distance. Here, the cluster-size formation is not only studied independently of the distance but also independently of the particle type and energy. The results of the cluster-size measurements and of Monte Carlo simulations are presented and discussed for 26.7 MeV ^{7}Li-ions, 16 MeV deuterons, 48 MeV ^{6}Li-ions and 96 MeV ^{12}C-ions, the last three ions all have the same specific energy of 8 MeV u^{-1} and therefore the same velocity, and for 20 MeV protons.

2. Particle track structure

As discussed in the introduction, the key for a general understanding of cellular responses is the track structure of ionizing radiation, which depends on the target medium and on the radiation quality of ionizing radiation. Here, the term 'track structure' indicates a detailed description of the interaction pattern of single ionizing particles when penetrating through matter, which is mainly determined by the properties of Coulomb interactions resulting in the excitation or ionization of the target molecules.

In this sense, each particle track j is defined by the set $\Omega^{(j)}$ of interaction points $t_i^{(j)}$, $i = 1, 2, \ldots$, of a particle in matter supplemented by the local energy deposits $\varepsilon_i^{(j)}$ transferred to matter at $t_i^{(j)}$, and by the type of atomic or molecular species $s_i^{(j)}$ possibly formed at these points due to the inelastic particle interactions of the primary particle and of all of its secondaries:

$$\Omega^{(j)} = \{t_i^{(j)}, i = 1,\ 2,\ \ldots;\ \varepsilon_i^{(j)},\ s_i^{(j)} \text{ energy deposited and species formed at } t_i^{(j)}\}. \quad (1)$$

In consequence, the structure of ionizing particles is characterized by the distance distribution of interaction points leading to specified effects like the ionization or excitation of target species. From the point of view of radiation damage to genes and living cells, the clustering of inelastic interaction points is of particular interest for target volumes, which are comparable in size with those of the most probable radiosensitive targets in biological systems (segments of DNA, chromatin fibre and nucleosomes).

Whereas the track structure of photons mainly consists of that of electrons, which are set in motion by photon interactions, like photoelectric absorption or Compton scattering, at interaction points the distances of which are generally much larger than the range of the electrons: the track structure of energetic ions is much more complex. It is characterized (i) by inelastic interactions of the primary particles along their path through matter forming the 'track core', and (ii) by inelastic interactions of secondary electrons (the δ-electrons), which are set in motion by impact ionization processes of the primary particles radially to the track core producing the so-called 'penumbra' region.

Here, the clustering of primary particle interaction points forming the track core is determined by the mean free path, λ_{in}, of the primary particles with respect to inelastic interactions, which depends strongly on the particles' charge state and on their velocity. Because of the interaction time available, the clustering generally increases with decreasing particle velocity due to the decreasing mean free path λ_{in}. Similarly, for primary particles at the same velocity, the clustering of inelastic primary interaction points within the track core increases

with the increasing charge state of the primary particles, because λ_{in} for a particle at charge state Z is expected within the framework of Bethe theory to scale with respect to the mean free inelastic path length for a proton $\lambda_{\mathrm{in}}^{(\mathrm{p})}$ according to $\lambda_{\mathrm{in}} = \lambda_{\mathrm{in}}^{(\mathrm{p})}/Z^2$.

In the same sense, the number of δ-electrons set in motion by primary particle interactions in a specified medium is characterized by the mean free path, λ_{ion}, of the primary particles with respect to impact ionization, which depends similarly on the particles' charge state and on its velocity as λ_{in}. With increasing particle velocity, λ_{ion} increases and, therefore, the number of δ-electrons taking part in the formation of a particle track segment decreases and leads to a less clustered ionization component of the particles' track core. At the same time, however, the energy distribution of δ-electrons forming the penumbra region is extended to higher energies, and thus leads to an enlargement of the lateral extension of the penumbra region because of the potential larger ranges of δ-electrons contributing to the particles' track structure.

The maximum energy, E_{max}, of a δ-electron set in motion by a primary particle at energy T and relative atomic mass M can be approximated, in the case of non-relativistic energies, as follows:

$$E_{\mathrm{max}} = \frac{4m_{\mathrm{el}}}{u} \times \left(\frac{T}{M}\right) \approx 2 \times 10^{-3} \times \left(\frac{T}{M}\right), \tag{2}$$

where m_{el} is the mass of an electron at rest, u is the atomic mass unit and (T/M) is the energy per nucleon of the primary particle. In consequence, the energy distribution of δ-electrons and, because of the range of the electrons at maximum energy, also the extension of the penumbra region are exclusively determined by the specific primary particle energy or by its velocity. Particles at the same specific energy are expected, therefore, to produce the same delta-ray spectrum with a linear number density that is proportional to Z^2, in accordance with Bethe theory.

Whereas the determination of a three-dimensional track-structure description according to equation (1) is possible by performing Monte Carlo simulations, it is not yet possible experimentally to determine the whole ensemble of single particle interaction points forming a particle track including the local energy deposits transferred to matter, and the atomic or molecular species induced at each point of particle interaction. It is, however, possible to measure the clustering of ionizing particle interactions in gaseous volumes of propane with sizes the masses per area of which are comparable with those of nanometre-sized volumes of liquid water as a substitute for the most radiation sensitive structures of cell nuclei, using low-energy electron counting techniques (De Nardo *et al* 2002a). Here, it is assumed (i) that the main features of particle track structure can be described by the frequency distribution of the number of ionizations (the so-called ionization cluster size), which are induced per primary particle in a specified nanometric target volume, V, and (ii) that frequency distributions of cluster size measured in propane at an appropriate gas pressure and volume size are equivalent to those induced by charged particles in nanometre-sized volumes of liquid water (Grosswendt 2004). In our case the target volume V has a cylindrical shape, with its main axis perpendicular to the particle beam direction.

The ionization component of particle track j in a detector volume V is given by the subset $\omega_{\mathrm{ion}}^{(j)} \subseteq \Omega^{(j)}$ that only includes those interaction points $t_i^{(j)}$, $i = 1, 2, \ldots$, which represent ionization processes and are located inside V:

$$\omega_{\mathrm{ion}}^{(j)} = \{t_i^{(j)}, i = 1, 2, \ldots; \varepsilon_i^{(j)}\text{energy deposited}, s_i^{(j)} \text{ ionized species at } t_i^{(j)} : t_i^{(j)} \in V\}. \tag{3}$$

Based on this definition, the ionization cluster size in volume V due to particle j corresponds to the number of elements $|\omega_{\text{ion}}^{(j)}|$ of subset $\omega_{\text{ion}}^{(j)}$. To analyse the ionization component of particle tracks, detectors must be used which are able to count the number of ionization interactions of a particle track within the detector volume. In addition, they must be small enough to resolve the spatial track structure, and they must be movable with respect to the particle trajectory to enable the measurement of cluster-size formation separately within the track core or within the penumbra region of a particle track.

To study the formation of ionization clusters produced by primary particles of radiation quality Q (particle mass, charge state and energy) in nanometre-sized volumes, (i) a well collimated particle beam is assumed that penetrates through or passes the target volume at a distance d to the centre of V, and (ii) an ionization counter is needed that is able to count the number of ions or electrons produced within the detector volume by each single particle of the beam (including those due to secondary electrons). This number of ions or electrons is then interpreted as the ionization cluster size. The result of the counting experiment for a large number N_{prim} of primary particles leads to a frequency distribution $N_\nu(Q; V)$, $\nu = 0, 1, 2, \ldots$, of ionization cluster size ν. Here, $N_\nu(Q; V)$ represents the frequency of particle histories with cluster size ν in the case of single ionizing particles of radiation quality Q. As zero events ($\nu = 0$) are included, the sum of $N_\nu(Q; V)$ over the recorded cluster sizes $\nu = 0, 1, \ldots, \nu_{\max}$ is equal to the number of particle tracks studied in the counting experiment:

$$N_{\text{prim}} = \sum_{\nu=0}^{\nu_{\max}} N_\nu(Q;V). \tag{4}$$

If the number of primary particles on which measurements are performed tends to infinity, the relative frequency $N_\nu(Q; V)/N_{\text{prim}}$ for the occurrence of cluster size ν tends to the probability distribution $P_\nu(Q; V)$ that exactly the number ν of ionizations is produced in the target volume by a particle of radiation quality Q. Because of the interpretation as a probability, the following conditions are valid for $P_\nu(Q; V)$:

$$0 \leqslant P_\nu(Q;V) \leqslant 1 \quad \text{for} \quad \nu = 0, 1, 2, \ldots \quad \text{and} \quad \sum_{\nu=0}^{\infty} P_\nu(Q;V) = 1. \tag{5}$$

In view of the fact that the probability distribution of cluster-size formation $P_\nu(Q; V)$, $\nu = 0, 1, 2, \ldots$, is related to ionization events within the tracks of single independent particles penetrating through or passing by a specified target volume, it describes the stochastic distribution of the ionization-cluster size of an average particle track. It takes into account the detector volume and the irradiation geometry but is independent of the absorbed dose implied to the target volume. In this sense, the cumulative distribution function $F_1(Q; V)$ defined by equation (6) gives the expectation value of the relative frequency that, due to ionizing interactions of a great number of single primary particles, at least, one ionization event takes place in the target volume.

$$F_1(Q;V) = \sum_{\nu=1}^{\infty} P_\nu(Q;V) = 1 - P_0(Q;V). \tag{6}$$

$F_1(Q; V)$ is, therefore, one of the probabilistic quantities that describes the radiation quality of an ionizing radiation.

The probability distribution of cluster-size formation $P_\nu(Q; V)$, $\nu = 0, 1, 2, \ldots$, strongly depends, of course, on the size of the target volume, V, and on the distance, d, between its

centre and the trajectory of a primary particle. If d is smaller than the volume's radius, R, the measured cluster-size distribution is related to the features of the track core of an ionizing particle, whereas it is related to the penumbra region if d is greater than R. The lateral extension of the penumbra region is exclusively determined by the ranges of δ-electrons set in motion by primary particles at maximum energy that, according to equation (2), only depends on the specific primary particle energy or on its velocity. In consequence, the lateral extension of the penumbra region of particles at the same specific energy but of different charge states is expected to be the same. In contrast, the number of δ-electrons, which are set in motion along a specified particle track segment and take part in the formation of the penumbra region, strongly depends on the particles' charge state. In the case of a short particle track segment, it is determined by the ratio of the segment length L to the particle's mean free ionization path length λ_{ion}, which is proportional to Z^2, in accordance with Bethe theory. For particles of the same charge state but at different specific energies, the penumbra region shows the largest lateral extension for the particle at greater specific energy because of the higher value of E_{max} and the resulting greater electron range. The number of δ-electrons taking part in the formation of the penumbra region, however, is higher for the particle at lower specific energy because of its smaller mean free ionization path length λ_{ion}.

3. Monte Carlo simulation of particle track structure

According to the definition of a particle track (see equation (1)) as the set of all interaction points of ionizing radiation in matter (including those of all of its secondary particles), the simulation of track structure by Monte Carlo methods requires the simulation of particle interaction processes from one interaction point to the other taking into account, as close as possible to reality, all kinds of interaction events necessary for track-structure analysis.

To calculate, for instance, the ionization component of the tracks of light ions (protons, α-particles and carbon ions) at specific energies of a few MeV u^{-1} during their penetration through material layers of small mass per area, it can be assumed that

(i) the energy loss due to impact ionization or excitation along short track segments does not appreciably change the initial particle energy,
(ii) the influence of elastic scattering on the particle energy and the flight direction can also be neglected in the case of short track segments,
(iii) the velocity of the primary particles is high enough to allow charge changing processes to be neglected.

In view of these assumptions, the simulation of the track structure of ionizing particles can be based exclusively on their ionization cross section, on the spectral and angular distribution of secondary electrons produced by impact ionization and on the properties of secondary electron degradation. The main steps for simulating their track segments are, therefore:

(i) the determination of the distance to the subsequent point of ionization impact interaction,
(ii) the determination of the energy and the direction of the secondary electron set in motion,
(iii) the simulation of electron transport.

As a consequence of this simulation strategy, the ionization pattern of a light-ion track segment can be subdivided into two contributions, the first one representing the ionization pattern

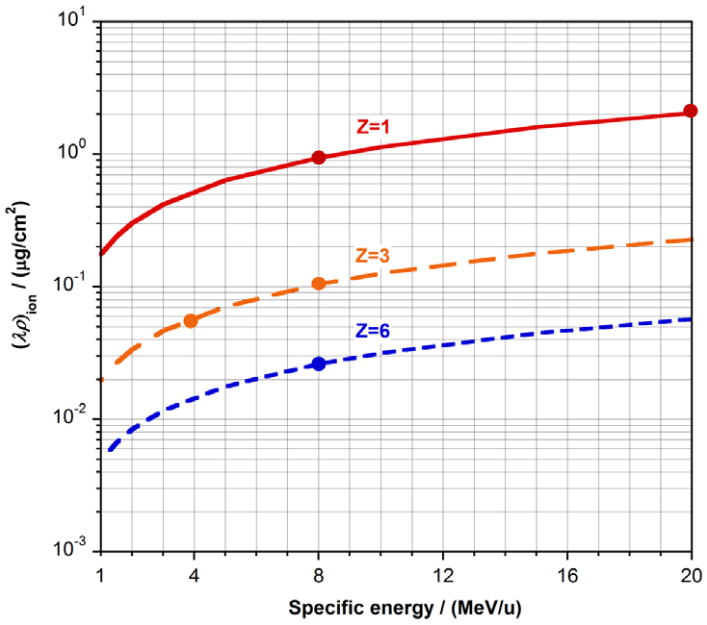

Figure 1. Mean free path for primary ionization $(\lambda\rho)_{\mathrm{ion}}$ in propane as a function of specific energy for $Z = 1$, $Z = 3$ and $Z = 6$ ions. Symbols point out charged particles investigated in this work: $Z = 1$: 8 MeV u^{-1} deuterons and 20 MeV u^{-1} protons; $Z = 3$: 3.81 MeV u^{-1} ^{7}Li-ions and 8 MeV u^{-1} ^{6}Li-ions; $Z = 6$: 8 MeV u^{-1} ^{12}C-ions.

directly produced by the light ions and the second one being that produced during degradation of secondary electrons if their initial energies are greater than 11.08 eV, which is the lowest ionization threshold energy of propane and rather close to the lowest ionization threshold energy of 10.78 eV in liquid water (for the equivalence of cluster-size distributions for propane and liquid water, see Grosswendt (2004) and Grosswendt *et al* (2004)).

3.1. Simulation of the track component due to primary particle interactions

On the condition that the track structure of protons and heavier particles is exclusively determined by primary impact ionization processes, the travelling distance l of a light ion at energy T between two successive interaction points is governed by an exponential probability density $f(l)$ which is completely determined by the mean free ionization path length $\lambda_{\mathrm{ion}}(T)$ of the light ion:

$$f(l) = \frac{1}{\lambda_{\mathrm{ion}}(T)} \times \mathrm{e}^{-\frac{l}{\lambda_{\mathrm{ion}}(T)}} \quad \text{with} \quad \lambda_{\mathrm{ion}}(T) = \frac{1}{\tilde{N} \times \sigma_{\mathrm{ion}}(T)}. \tag{7}$$

Here, $\tilde{N}$ is the number density of target atoms or molecules and $\sigma_{\mathrm{ion}}(T)$ the ionization cross section for a primary light ion at energy T.

To give an impression of the mean free ionization path length of light ions in propane, figure 1 shows the mass per area $(\lambda\rho)_{\mathrm{ion}}$ for ionizing particles of charge state $Z = 1$, 3 and 6, respectively, as a function of the specific energy of the primary particles studied in this work (for the cross sections used to calculate $\lambda_{\mathrm{ion}}(T)$, see De Nardo *et al* (2002a)). At first glance,

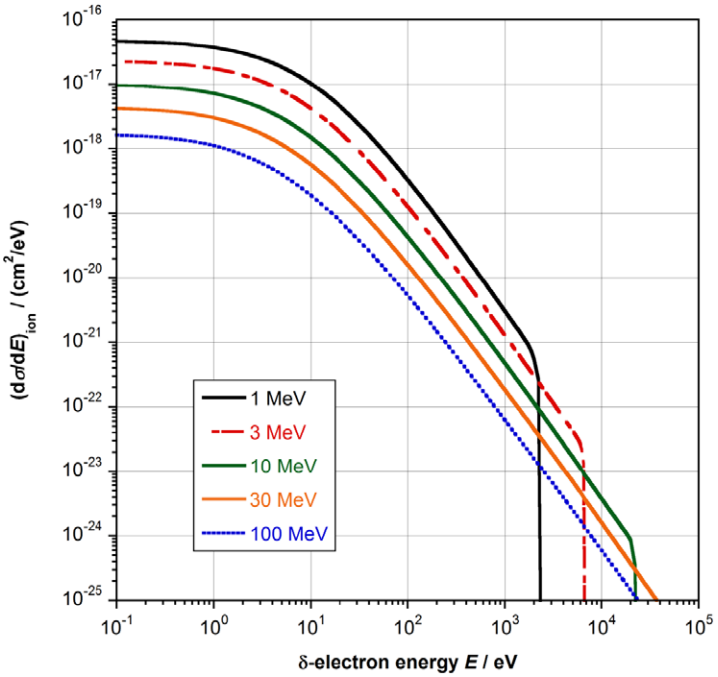

Figure 2. Spectral distribution of δ-electrons set in motion in propane by protons at different energies.

the increase of $(\lambda\rho)_{\text{ion}}$ with increasing specific energy is obvious, and clearly demonstrates the decreasing particle interaction probability with increasing particle velocity. In addition, the scaling of $(\lambda\rho)_{\text{ion}}$ with $1/Z^2$ for particles at the same velocity or specific energy is also obvious from the figure.

The energy E of secondary electrons is calculated on the basis of the single-differential ionization cross section with respect to E by using the semi-empirical Hansen–Kocbach–Stolterfoht (HKS) model (ICRU 1996) and a random number η which is homogeneously distributed between 0 and 1:

$$\eta = F[f(E)] = \frac{1}{\sigma_{\text{ion}}(T)} \int_0^{E(T)} \left(\frac{\mathrm{d}\sigma(T)}{\mathrm{d}E'}\right)_{\text{ion}} \mathrm{d}E' \quad \text{with} \quad 0 \leqslant E(T) \leqslant E_{\max}. \tag{8}$$

For non-relativistic energies, $E_{\max}$ is given by equation (2). Here, $F[f(E)]$ is the probability that in an ionizing interaction the energy of a secondary electron set in motion by impact ionization is less than or equal to $E(T)$.

To apply the HKS-model to propane, the necessary electron binding energies and occupation numbers of the model of Hwang *et al* (1996) are used, which assumes for propane ten orbitals of outer or weakly bound valence electrons.

The typical shape of the energy distribution of δ-electrons set in motion in propane by protons is presented in figure 2 for primary particles at energies between 1 and 100 MeV by displaying the energy-differential ionization cross section, $(\mathrm{d}\sigma/\mathrm{d}E)_{\text{ion}}$, as a function of the δ-electron energy E. Independently of the primary particle energy, the double-logarithmic plot of $(\mathrm{d}\sigma/\mathrm{d}E)_{\text{ion}}$ shows a more or less constant value up to about 1 eV followed by a nonlinear

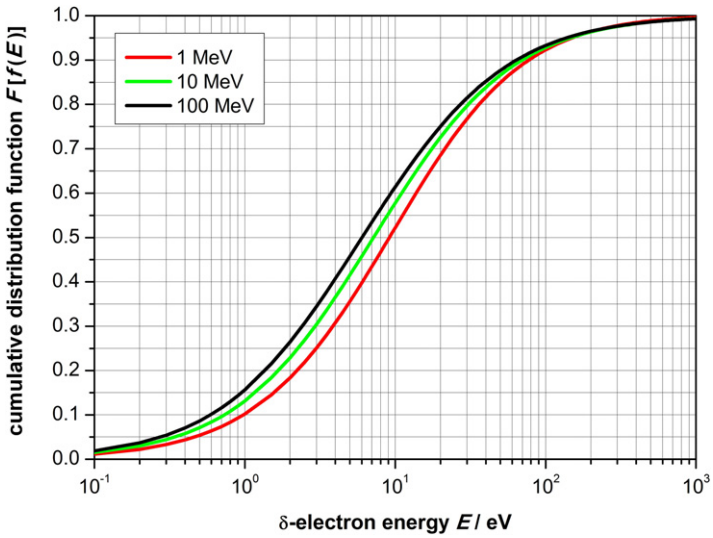

Figure 3. Probability that in an ionizing interaction the energy of a secondary electron set in motion by impact ionization of protons in propane is less than or equal to E.

decrease with increasing δ-electron energy until the typical $1/E^2$-dependence of the δ-electron distribution is reached. The main differences between the distributions for different proton energies are (i) the decreasing absolute values with increasing proton energy at the same δ-electron energy and (ii) the maximum possible electron energy, which increases with increasing proton energy according to equation (2).

Because of the fact that the interaction cross sections of particles at charge state Z are proportional to Z^2 and do not depend on kinetic energy but on the velocity, the shape of the energy distribution of δ-electrons set in motion by particles at charge state Z in propane is the same as that of protons at the same velocity but with absolute values multiplied by Z^2.

In view of the high values of $(\mathrm{d}\sigma/\mathrm{d}E)_{\mathrm{ion}}$ for δ-electron energies $E \leqslant 10$ eV, a large fraction of the secondary electrons set in motion by impact ionization is not able to induce further ions as their energy is less than the lowest ionization threshold energy of propane. To demonstrate this fact in greater detail, figure 3 shows the probability $F[f(E)]$, which is defined in equation (8), that in an ionizing interaction of protons at energies between 1 and 100 MeV in propane the energy of δ-electrons is less than or equal to E. For protons at 1 MeV, for instance, the fraction of δ-electrons at energies $E \leqslant 10$ eV is about 52% and that at energies $E \leqslant 100$ eV about 92%, whereas for protons at 100 MeV the corresponding δ-electron fractions are about 62 and 93%, respectively. Generally it can be seen in the figure that 95% of δ-electrons have energies of less than about 150 eV.

3.2. Simulation of the track component due to secondary electrons

To get a realistic image of the ionization pattern produced by electrons in propane, the history of an electron must be followed from one interaction point to the other, taking all relevant electron interaction processes into account. The main steps for simulating the penetration of electrons

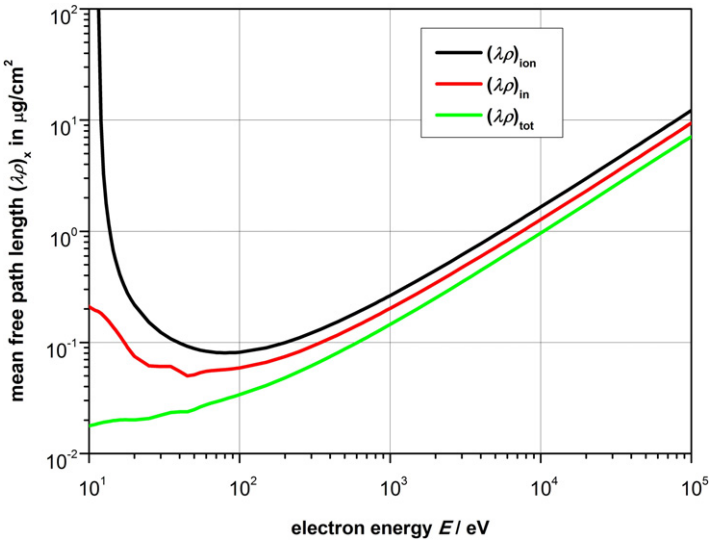

Figure 4. Mean free path lengths of electrons in propane with respect to ionization, inelastic scattering and total scattering as a function of energy E.

through matter are, therefore:

(i) the determination of the distance to the subsequent electron interaction point, taking into account elastic and inelastic scattering processes,

(ii) the determination of the type of interaction the electron suffers at this point, including all relevant atomic or molecular excitation and ionization processes,

(iii) the sampling of the energy loss and the new flight direction due to the selected interaction process, possibly supplemented by the energies and flight directions of secondary particles.

Analogously to the travelling lengths of ions, the distance $l(E)$ an electron at energy E covers to reach the subsequent interaction point is governed by the exponential probability density $f(l) = \exp\{-l/\lambda_{tot}(E)\}/\lambda_{tot}(E)$, which is completely determined by the mean free total scattering path length $\lambda_{tot}(E)$ of the electron.

Here, the mean total electron scattering path length $\lambda_{tot}(E)$ is given by $[\tilde{N}\sigma_{tot}(E)]^{-1}$, where $\tilde{N}$ is again the number density of the target atoms or molecules and $\sigma_{tot}(E)$ the total scattering cross section for an electron at energy E. The latter is given by the sum over the elastic cross section and over all the available inelastic cross sections (see De Nardo *et al* 2002a).

For more details on the simulation of the track component due to secondary electron interactions and for the reliability of the used set of electron cross sections, see again De Nardo *et al* (2002a).

The ionization cluster-size distributions are calculated according to the counting experiment defined above by the simulation of the tracks of a large number of primary particles, and counting either the number of ions or low-energy electrons which appear in a specified detector volume, taking into account the main properties of the detector.

To give an impression of these cross sections, figure 4 shows the mean free path lengths of electrons in propane with respect to ionization, $(\lambda\rho)_{ion}$, inelastic scattering, $(\lambda\rho)_{in}$, and total scattering, $(\lambda\rho)_{tot}$, expressed in mass per area, as a function of electron energy.

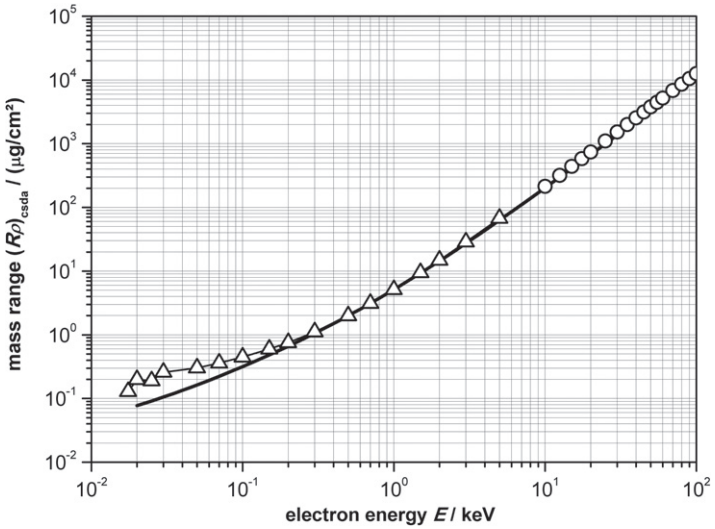

Figure 5. Mass range ($R\rho$) of electrons in propane as a function of their energy E: triangles with thin line, mean total travelling length of electrons in propane calculated by Monte Carlo simulation; circles, continuous-slowing-down mass ranges (ESTAR); thick line, data published by Cole (1969) for air adapted to propane by multiplication with the mass-stopping-power ratio $S_m^{(air)}/S_m^{(propane)}$ at 10 keV (ESTAR).

A first glance at the figure immediately demonstrates that the mean free path lengths of electrons at energies less than 10 keV are comparable with the ionization path lengths of light ions presented in figure 1. Whereas the mean free ionization path length $(\lambda\rho)_{ion}$ shows a rather high value at 12 eV, then decreases with increasing electron energy down to a minimum at about 80 eV, and increases afterwards if the energy is further increased, the mean free total path length $(\lambda\rho)_{tot}$ increases almost continuously with increasing electron energy and the mean free path length $(\lambda\rho)_{in}$ for inelastic scattering shows an energy dependence in between. The increasing difference between $(\lambda\rho)_{in}$ and $(\lambda\rho)_{tot}$ with decreasing electron energy clearly demonstrates the increasing importance of elastic electron scattering and the same dependence of $(\lambda\rho)_{ion}$ and $(\lambda\rho)_{in}$ as a function of energy leads to the constancy of electron W-values at higher electron energies (ICRU 1979).

To give an impression of the potential extension of the track component due to secondary electrons, figure 5 shows the mean total travelling length of electrons as a function of their energy, calculated by Monte Carlo simulation for energies less than 5 keV using the model just described. These data are compared with the continuous-slowing-down ranges of NIST (ESTAR), and with the data of Cole (1969) for air adapted to propane by multiplication with the mass stopping power ratio $S_m^{(air)}/S_m^{(propane)}$ at 10 keV (ESTAR). A first glance at the figure shows a very satisfactory agreement between the different data sets, at least, at energies greater than about 200 eV. The deviations at smaller energies are due to the fact that the data published by Cole do not represent total travelling lengths but projected ranges.

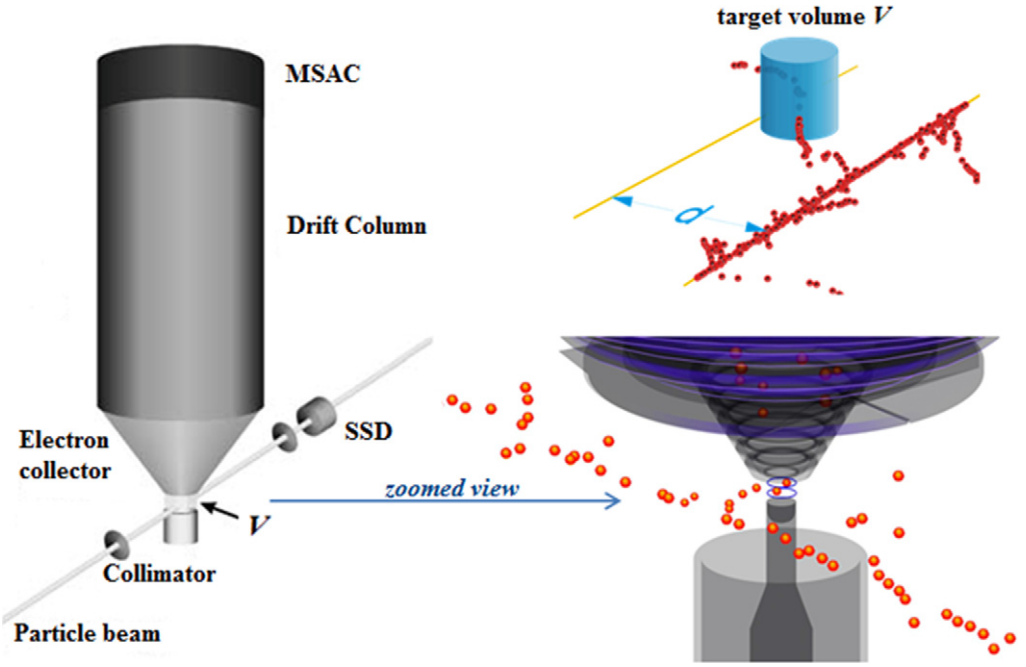

Figure 6. Schematic view of the track-detector. The ions of a collimated narrow beam pass the target volume V and are detected by a solid-state detector (SSD), which triggers the data acquisition; electrons produced at the passage of each ion within V are collected into a single-electron counter, which consists of a drift column and a MSAC, and are detected as a function of their time of arrival at the MSAC.

4. Experiment

4.1. Experimental set-up and method

We conceived and developed an experimental apparatus, able to count the number of ionizations produced by single light ions within a nanometre-sized volume V when they cross or pass by the target volume at a specified distance. The apparatus is installed at the +50° beam line of the Tandem–Alpi accelerator complex at the INFN—Legnaro National Laboratories. It basically consists of a vacuum chamber, at a pressure of 10^{-6} mbar, and an interaction chamber, filled with propane gas at 3 mbar, separated by a 1.5 μm aluminized Mylar window. The vacuum chamber contains a beam profile detector to control the shape and intensity of the ion beam (De Nardo *et al* 2007). The interaction chamber contains the main detector (the track-detector), a silicon trigger detector, different collimators and a movable alpha-particle ^{244}Cm source, used for calibration. The main components of the track-detector are the target volume V, the electron collector, the drift column and a multi-step avalanche chamber (MSAC) placed on the top of the drift column. The target volume V is an almost wall-less cylinder 3.7 mm in diameter and height. At 3 mbar of propane gas the diameter $(D\rho)_V$ of the volume V is about 2 μg cm^{-2} in mass per area (ρ is the propane gas density), which corresponds to a length of 20 nm when scaled at a density of 1 g cm^{-3}. A schematic view of the measuring arrangement is given in figure 6.

The cross section of the ion beam is defined by several collimators, which are 0.8 mm in diameter. The detector is mounted on a movable platform, allowing the positioning of the target volume V at different impact parameters d with respect to the primary ion trajectory, with an accuracy of 0.1 mm. The vertical axis of the volume V is perpendicular to the central line of the particle beam. More details on the track-detector can be found in De Nardo *et al* (2002b).

Slow electrons appearing inside V at the passage of each primary particle are sucked into a long drift column by means of a static electric field properly shaped by several mini electrodes (composing the so-called electron-collector). While drifting along the column the electrons diffuse and finally reach the MSAC at different times. Each electron at the MSAC gives rise to a pulse whose height is distributed according to a Polya distribution (Conte *et al* 2010). At the passage of each primary particle impinging the silicon detector, a trail of pulses is recorded, and each pulse above the noise level is counted as an electron. The trigger signal is delayed so that the arrival time of these electrons at the MSAC is Gaussian distributed around a mean value of about 8 μs (depending on the trigger signal timing, on the length of the drift column and on the electrons' drift velocity) with a full-width at half-maximum of about 1.6 μs.

Waveforms of 16 μs length are sampled at a frequency of 5×10^8 s^{-1} by a PCI analogue to digital acquisition board and stored for off-line processing. To increase the signal-to-noise ratio, correlation techniques are applied off-line to the raw pulse trails, then a selective time window is applied in order to eliminate all the waveforms containing pulse trails that are not consistent with the expected electron arrival-time distribution. Remaining pulses are counted one by one in each waveform and an ionization cluster-size distribution is generated.

Track-structure measurements are affected by a background contribution from spurious pulses, like those due to false coincidences by cosmic rays (De Nardo *et al* 2002a). In order to reduce this background, at each impact parameter two sets of measurements are always performed (one that includes the information from track structure and another that only includes the background), and an unfolding procedure is applied to the measured cluster-size distributions. See the publication of Conte *et al* (2010) for details on the data processing procedure.

As demonstrated by Grosswendt (2004) and Grosswendt *et al* (2004), cluster-size distributions obtained in a propane filled cylinder are equivalent to those produced in a water cylinder, the diameter of which is equal to that of a propane cylinder divided by 0.8. At 3 mbar of propane gas the diameter of our target volume V has a mass per area of about 2 μg cm^{-2}, which corresponds to a length of 20 nm at a density of 1 g cm^{-3}. Therefore our detector measures cluster-size distributions equivalent to those for a liquid water cylinder 25 nm in diameter.

4.2. Detector efficiency

The track-detector efficiency ε for single-electron detection is the product of three factors: the efficiency ε_V for electron transfer from the volume V into the detector system, the efficiency $\varepsilon_{\text{drift}}$ for electron transfer through the drift column and the efficiency $\varepsilon_{\text{MSAC}}$ for single-electron detection at the MSAC: $\varepsilon = \varepsilon_V \times \varepsilon_{\text{drift}} \times \varepsilon_{\text{MSAC}}$. The collection efficiency ε_V is not uniform inside V but it decreases with increasing distance both from the 3.7 mm diameter hole connecting the electron collector to V and from the central axis of the cylinder. To get a complete map of the efficiency, the product $\varepsilon_V \times \varepsilon_{\text{drift}}$ was calculated with a Monte Carlo code by simulation of the electron transport through the counter, from within the target volume to

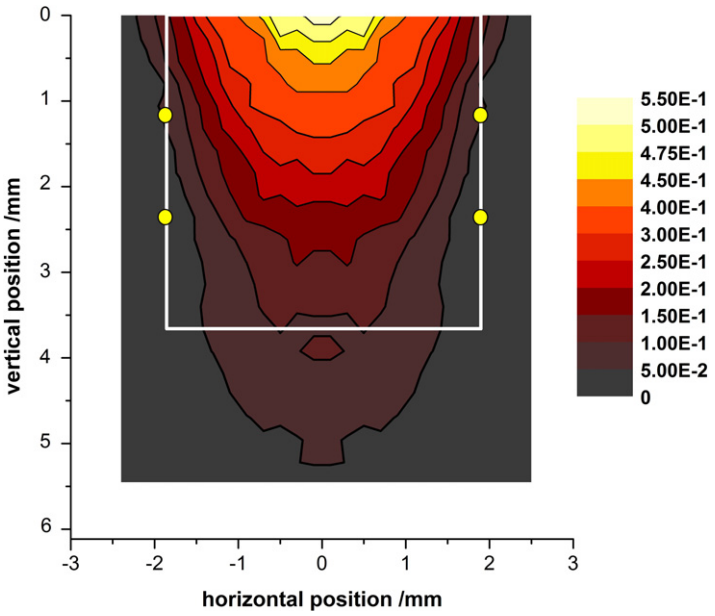

Figure 7. Colour-coded contour plot of the efficiency map $\varepsilon_V \times \varepsilon_{\text{drift}}$ that describes the probability that a slow electron from position (X, Y) is detected by the single-electron counter at the MSAC. The white square represents the 'nominal' cylindrical target volume V of 3.7 mm in width and 3.7 mm in height. The yellow circles represent the confining electrode rings of 0.1 mm in diameter.

the end of the drift column (De Nardo *et al* 2002b). A picture of the efficiency map concerning $\varepsilon_V \times \varepsilon_{\text{drift}}$ is given in figure 7.

A slow electron at position (0 mm, 0 mm), for example, is detected with an efficiency between 50 and 60% while a slow electron at position (1.3 mm, 1.3 mm) is detected with an efficiency slightly higher than 20%. By assuming a uniform electron distribution inside V, the mean value of the product $\varepsilon_V \times \varepsilon_{\text{drift}}$ is about 18%.

Provided that the gas gain of the MSAC is constant, the detection efficiency $\varepsilon_{\text{MSAC}}$ of the single electron at the MSAC, defined as the fraction of signals that are above the electronic noise threshold, depends on the noise level. It was estimated in previous measurements performed in the laboratory to be about 98%, but in the accelerator environment the electronic noise is much higher than before, consequently the efficiency of the single-electron detection $\varepsilon_{\text{MSAC}}$ at the MSAC has been measured to be about 90%.

The efficiency map of single-electron detection was also taken into account in the Monte Carlo simulation, and consequently the measured and simulated electron cluster-size distributions include the efficiency ε as a parameter and are indicated by $P_\nu(Q, V, \varepsilon)$.

In addition to the efficiency of single-electron detection, the efficiency to count properly several electrons belonging to the same cluster size is also limited by the time resolution of the detector, which is the capability to distinguish and count separately electrons arriving one after the other. Here, it can be assumed that, with increasing cluster-size, the probability increases that two or more electrons reach the MSAC almost simultaneously, and are not counted separately but as one electron only. As mentioned above, the arrival time of the electrons is Gaussian distributed with a standard deviation of about 700 ns. Considering a resolving time

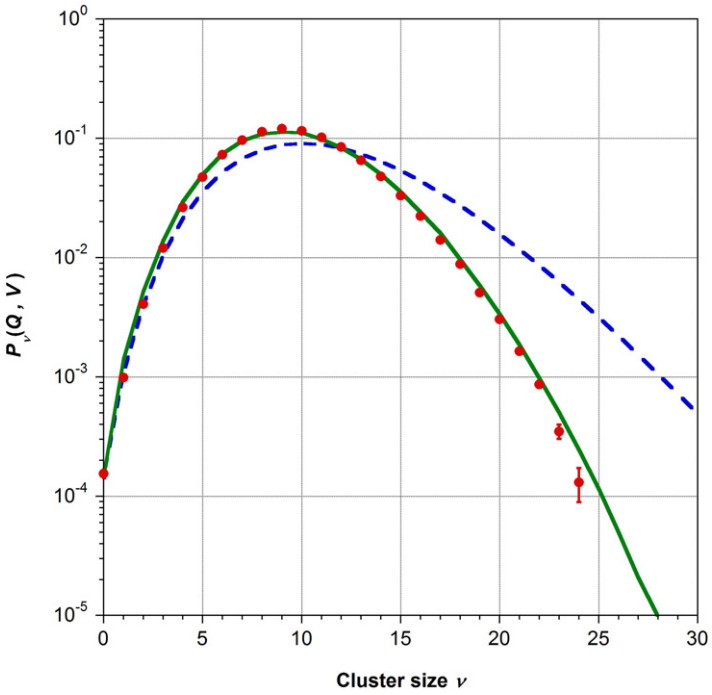

Figure 8. Cluster-size distribution due to 26.7 MeV ^{7}Li-ions at impact parameter $d\rho = 0\,\mu\mathrm{g\,cm^{-2}}$: symbols, experimental data; broken line, Monte Carlo simulations taking into account the single-electron detection efficiency; continuous line, Monte Carlo simulations after taking into account the single-electron detection efficiency and the transformation according to equation (9) with $\tau = 30$ ns. Uncertainty bars only take the statistics into account.

$\tau = 30$ ns, given mainly by the width of the single-electron pulse, we calculated the efficiency $\varepsilon_{\nu,\mu}(\sigma, \tau)$ of the detector in resolving a number of ν (with $\nu \leqslant \mu$) out of μ electrons (De Nardo *et al* 2006). As a consequence, the distribution $P_\nu(Q,\ V,\ \varepsilon)$ is transformed for all values of ν to $P_\nu(Q,\ V;\ \mathrm{exp})$:

$$P_\nu(Q, V; \mathrm{exp}) = \sum_{\mu=\nu}^{\infty} P_\mu(Q, V, \varepsilon) \cdot \varepsilon_{\nu,\mu}(\sigma, \tau) \tag{9}$$

with the condition

$$\sum_{\nu=1}^{\mu} \varepsilon_{\nu,\mu}(\sigma, \tau) = 1 \quad \text{for } \mu = 1, 2, 3, \ldots \tag{10}$$

It can be noticed that the only possibility to count $\nu = 0$ electrons is for $\mu = 0$, and therefore $\varepsilon_{0,\mu}(\sigma, \tau) = \delta_{0\mu}$ (Kronecker delta). For simplicity of notation, $P_\nu(Q, V; \mathrm{exp})$ is indicated in the following as $P_\nu(Q,\ V)$.

To compare experimental with simulated results, equation (9) was also applied to the Monte Carlo distributions, which did not take into account the time resolution of the track-detector.

As an example, in figure 8 the experimental cluster-size distribution due to 26.7 MeV ^{7}Li-ions at impact parameter $d\rho = 0\,\mu\mathrm{g\,cm^{-2}}$ is plotted together with the Monte Carlo distribution,

Table 1. Primary particle type, energy and specific energy are given for all ions investigated in this work, supplemented by maximum energies of δ-electrons, calculated according to equation (2), by the penumbra radius $(R\rho)_P$ as given by the continuous-slowing-down mass range in propane (ESTAR) and by the ionization mean free path $(\lambda\rho)_{ion}$ of the particles (see figure 1).

Primary particle	Energy (MeV)	Specific energy (MeV u^{-1})	Max energy of $\boldsymbol{\delta}$-electrons (keV)	Penumbra radius $(\mathbf{R}\rho)_{\mathbf{p}}$ (μg cm^{-2})	$(\boldsymbol{\lambda\rho})_{ion}$ (μg cm^{-2})
^{1}H	20	20	44	3000	2.05
^{2}H	16	8	17	600	0.941
^{6}Li	48	8	17	600	0.105
^{7}Li	26.7	3.81	7	113[a]	0.055
^{12}C	96	8	17	600	0.026

[a] Found by linear extrapolation in the double $\log_{10}$ scale of $(R\rho)_P$ using the ESTAR data between 20 and 10 keV.

which only takes into account the single-electron detection efficiency-map, and with the Monte Carlo distribution after its transformation according to equation (9).

Without taking into account the time resolution of the detector, the agreement between the experimental and the Monte Carlo distribution is rather poor at large cluster-sizes, but it becomes very satisfactory if the time resolution is taken into account.

4.3. Measurement plan

To study the track-structure characteristics of several light ions we measured and calculated the cluster-size distributions for 20 MeV protons, 16 MeV deuterons, 48 MeV ^{6}Li-ions, 26.7 ^{7}Li-ions and 96 MeV ^{12}C-ions (for further details, see table 1), at different impact parameters d of the primary ion trajectories with respect to the centre of the target volume V. To study separately the track-core region and the penumbra region of particle tracks, the impact parameter d was changed between 0 and 8 mm, which corresponds to a maximum distance with a mass per area of about 4.1 μg cm^{-2} and is almost equal to the continuous-slowing-down mass range of 850 eV electrons in propane (see figure 5).

The lateral extension of the penumbra region is determined by the maximum energy of δ-electrons set in motion by primary particles, which depends only on their velocity. For example, the maximum energy of δ-electrons set in motion by 20 MeV protons is about $E_{max} = 44$ keV, whereas for 26.7 MeV ^{7}Li-ions it is $E_{max} = 7$ keV; the penumbra radii are, therefore, about 3 and 0.113 mg cm^{-2}, respectively (see table 1).

Despite the fact that the penumbra radius seems to extend to large values, it should be kept in mind that only a very few electrons have enough energy to reach that distance. To demonstrate this fact in detail, figure 9 shows the highest electron energy that corresponds either to a fraction of 99, 99.9 and 99.99% of all δ-electrons set in motion by protons in propane as a function of proton energy, as a result of the data presented in figure 3. If we consider 20 MeV protons, for instance, the fraction of δ-electrons that have energies greater than 16.5 keV is less than 10^{-4}, that of δ-electrons with energies greater than 5 keV is less than 10^{-3} and the δ-electron fraction with energies greater than 700 eV is about 10^{-2}, which corresponds to a range of about 3.5 μg cm^{-2}.

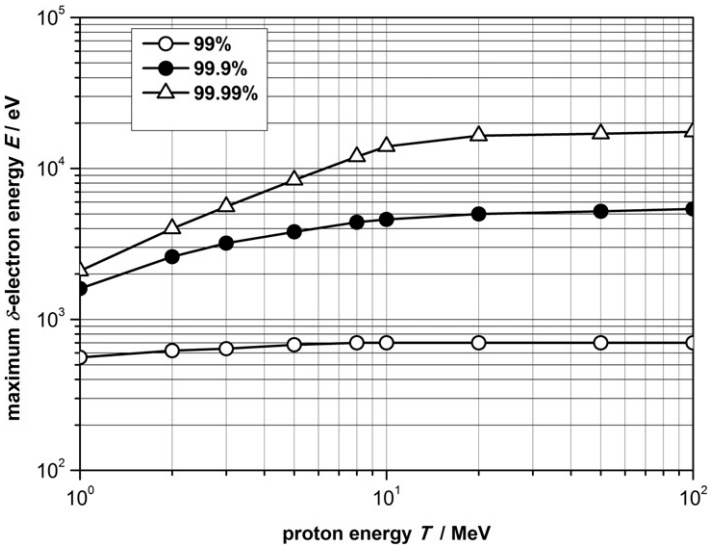

Figure 9. The highest electron energy which corresponds to a fraction of 99% (open circles), of 99.9% (closed circles), or of 99.99% (open triangles) of all electrons, as a function of primary proton energy.

Therefore, even if the penumbra radius $(R\rho)_{\mathrm{P}}$ for 20 MeV protons is as large as 3 mg cm^{-2} (30 μm at unit density, or about 5.5 m at a propane gas pressure of 3 mbar at 25 °C) the region is much smaller in which the electron density is high enough to give a significant contribution to the structure of particle tracks. In general it can be stated that 99% of all ionizing collisions describing the track structure take place within a mass per area of about 3.5 μg cm^{-2} (35 nm at unit density, 6.5 mm at a propane gas pressure of 3 mbar at 25 °C).

Whereas the spectral distribution of induced δ-electrons and the extension of the penumbra region of the track structure are the same for the different types of primary particles moving at the same velocity, the number of δ-electrons set in motion along a specified track segment strongly depends on the particles' charge state, and is determined by the ionization mean free path length $(\lambda\rho)_{\mathrm{ion}}$ of the primary particles in propane. For 16 MeV deuterons it is about 1 μg cm^{-2}, for 48 MeV ^{6}Li-ions about 0.1 μg cm^{-2}, and for 96 MeV ^{12}C-ions about 0.03 μg cm^{-2}, which corresponds to 10, 1 and 0.3 nm at a target density of 1 g cm^{-3}.

In order to estimate how many primary particles are required for a statistically significant measurement, we must keep the statistical uncertainty of the relative frequency of non-zero track-events $F_1(Q, V)$ (see equation (6)), comparable to other experimental uncertainties of about 1%. In consequence, the number of primary particles N_{prim} multiplied by $F_1(Q, V)$ must be at least 10^4. Due to the fact that $F_1(Q, V)$ depends on the Z value and the velocity of the investigated ions, as well as on the impact parameter d, the number N_{prim} must be chosen appropriately. When a primary particle directly passes through the target volume V at its centre, the mean number of ionizing collisions along the primary trajectory is given by the ratio $(D\rho)_V/(\lambda\rho)_{\mathrm{ion}}$. If the primary particles are ^{12}C-ions at an energy of 96 MeV ($(\lambda\rho)_{\mathrm{ion}} = 0.026\,\mu$g cm^{-2}) this ratio is equal to about 80, which means that each ion produces with high probability at least one detectable ionization inside V, and in consequence 10^4 particles are enough to get 10^4 non-zero track-events. In contrast, for low Z and relatively fast primary particles, like 20 MeV protons ($(\lambda\rho)_{\mathrm{ion}} = 2.05\,\mu$g cm^{-2}), the mean number of ionizing

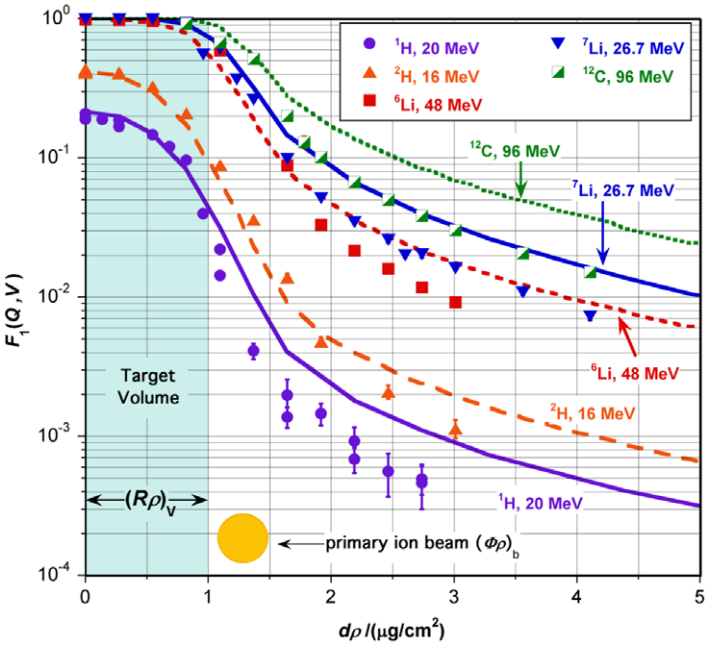

Figure 10. The cumulative distribution function $F_1(Q, V)$ as a function of the impact parameter $d\rho$, for ions of different qualities, as specified in the inset. Symbols relate to measurements, lines to Monte Carlo simulations. Only statistical uncertainties are plotted.

collisions is about 1, therefore, taking into account an average detection efficiency of about 20%, it means that the majority of tracks leads to a cluster-size zero, and consequently the number of protons at the trigger detector must be correspondingly higher than 10^4. The situation is even worse if the primary particle does not cross the target volume V directly but passes by with a large impact parameter, in which case the only ionizing contribution is that due to energetic δ-electron emerging from the track core.

At the explored distances d from the primary trajectory, the density of δ-electrons decreases mainly due to geometrical reasons, therefore roughly as d^{-2}, and the number of collected events should increase accordingly. Unfortunately, due to beam time restrictions, it was not always possible to acquire as many primary particles as required. Because of this, the number of particle tracks ranged from a minimum of 10^4 for 96 MeV ^{12}C-ions directly traversing V, up to a maximum of 5×10^6 tracks at the largest impact parameter.

5. Results

5.1. Relative frequency of ionizing events

As a first result, figure 10 shows the cumulative distribution function $F_1(Q, V)$ defined by equation (6), which represents the relative frequency of ionizing events in the target volume V, as a function of the impact parameter $d\rho$ for different ions of quality Q. Both experimental and simulated values are shown.

The 20 MeV protons are the ions of lowest Z and highest velocity, while the 16 MeV deuterons ($Z = 1$), the 48 MeV ^{6}Li ($Z = 3$) and the 96 MeV ^{12}C ($Z = 6$) ions, move at the same velocity but have increasing Z values.

It is worth remembering that the primary ion beam has a diameter $(\Phi\rho)_b$ of about $0.4\,\mu g\,cm^{-2}$, and the target volume V has a radius $(R\rho)_V$ of about $1\,\mu g\,cm^{-2}$, which corresponds approximately to the range of 250 eV electrons (see figure 5).

For all the ions the function $F_1(Q, V)$ shows similar behaviour: it has a maximum at $d\rho = 0\,\mu g\,cm^{-2}$ if the ion directly crosses the target volume V at its centre, and it decreases with increasing impact parameter. For $d\rho < (R\rho)_V$, the ionizations directly produced by the primary ion are included in $F_1(Q, V)$; since each ion produces with high probability an ionization inside V, $F_1(Q, V)$ reaches almost 1, with the only exception of protons and deuterons which have a lower ionization cross section and a correspondingly lower linear ionization density inside V. $(\lambda\rho)_{ion}$ being the ionization mean free path of the ion and $(D\rho)_V$ the diameter of the target volume V, it can be estimated that each ion produces, inside V, an average number of ionizing collisions equal to the ratio $(D\rho)_V/(\lambda\rho)_{ion}$. As already reported in table 1, 20 MeV protons and 16 MeV deuterons have ionization mean free path length $(\lambda\rho)_{ion}$ equal to 2.05 and $0.941\,\mu g\,cm^{-2}$, respectively, that is comparable with the diameter of the target volume V (about $2.0\,\mu g\,cm^{-2}$). Therefore, the expected number of ionizing collisions inside the target volume V is $(D\rho)_V/(\lambda\rho)_{ion} = 0.98$ for 20 MeV protons, and $(D\rho)_V/(\lambda\rho)_{ion} = 2.1$ for 16 MeV deuterons. Taking into account that the overall single-electron-detection efficiency is about 20%, it turns out that for protons the cumulative probability to measure an ionizing interaction inside V is about 0.2, while it is about 0.4 for 16 MeV deuterons, in good agreement with both experimental and calculated data.

On the other hand, for ^{6}Li-ions at 48 MeV, $(\lambda\rho)_{ion}$ is only $0.105\,\mu g\,cm^{-2}$ and consequently the average number of ionizing collisions rises to $(D\rho)_V/(\lambda\rho)_{ion} = 19$. Even reduced by the detector efficiency, in this case the measured cumulative ionization frequency $F_1(Q, V)$ has to be close to 1, and indeed it is. The same is obtained for ions having a still higher linear ionization density, namely 26.7 MeV ^{7}Li-ions and 96 MeV ^{12}C-ions.

For $d\rho < (R\rho)_V + 0.5 \times (\Phi\rho)_b$, $F_1(Q, V)$ decreases with increasing $d\rho$, mainly due to the shortening of chord lengths $(l\rho)_V$ and also to the decreasing detector efficiency (see figure 7). Between $d\rho = 1\,\mu g\,cm^{-2}$ and about $1.2\,\mu g\,cm^{-2}$ the decrease is very steep, corresponding to the exit of the beam from V.

For all the ions $F_1(Q, V)$ decreases with increasing distance $d\rho$ approximately as $(d\rho)^{-2}$ which corresponds to the decrease of the solid angle. Similar results were obtained with larger target volumes (Schmollack *et al* 2000).

For ions moving at the same velocity λ_{ion} scales as Z^{-2} and consequently the number of δ-electrons reaching the target volume V in the penumbra region (and thus also $F_1(Q, V)$) increases according to Z^2. If the particle velocity increases, λ_{ion} also increases and, therefore, the number of δ-electrons set in motion along the primary track decreases. This explains why the values of $F_1(Q, V)$ for 20 MeV protons are smaller than those for 16 MeV deuterons.

In the penumbra region for $d\rho > 1.5\,\mu g\,cm^{-2}$, the experimental results are systematically lower than the corresponding simulated data. On the one hand this might be due to the absorption of δ-ray electrons by two electrode rings that are confining the target volume V and are not included in the simulated geometry of Monte Carlo calculations (see figure 7); on the other hand it could be due to deficiencies of the Monte Carlo simulations with respect to the applied interaction cross sections, which may affect the cluster-size distributions simulated by

Table 2. Values of the fitting parameters A and B of the power function $F_1(Q, V) = A \times [d\rho/(R\rho)_V]^{-B}$ for primary particles of mean free ionization path length $(\lambda\rho)_{\text{ion}}$.

Primary particle	Energy (MeV)	Ionization mean free path$(\lambda\rho)_{\text{ion}}$ (μg cm^{-2})	Mean number of ionizations produced along D $(D\rho)_V/(\lambda\rho)_{\text{ion}}$	Factor A	Exponent B
^{1}H	20	2.05	0.975	0.0062[a]	2.57[a]
				0.0095[b]	2.13[b]
^{2}H	16	0.941	2.13	0.022[a]	2.49[a]
				0.021[b]	2.14[b]
^{6}Li	48	0.105	19.1	0.18[a]	2.71[a]
				0.20[b]	2.18[b]
^{7}Li	26.7	0.055	36.4	0.25[a]	2.49[a]
				0.39[b]	2.28[b]
^{12}C	96	0.026	76.5	0.48[a]	2.48[a]
				0.72[b]	2.13[b]

[a] Fit of experimental data.
[b] Fit of Monte Carlo results.

Monte Carlo methods (Gargioni and Grosswendt 2007). This latter assumption is also supported by the fact that similar differences were also observed for cluster-size distributions measured with ion-counting nanodosimeters and compared with distributions simulated by Monte Carlo codes based on the same physical assumptions and approximations (Garty *et al* 2002a, 2002b, Bantsar *et al* 2004, Wroe *et al* 2006, Hilgers *et al* 2007).

For larger distances, $d\rho > (R\rho)_V + 0.5 \times (\Phi\rho)_b$, the contribution to $F_1(Q, V)$ is exclusively determined by δ-electrons that are able to reach the target volume V. The number of these electrons mainly depends on the mean free ionization path length of the primary particles and on the solid angle of the target volume seen from the point of setting in motion of the electrons, but also on their spectral distribution, which only contains a few electrons with a long range (see figure 3).

To study the properties of $F_1(Q, V)$ in the penumbra region in greater detail, figures 11(a) and (b) present the measured and calculated values of $F_1(Q, V)$ as a function of $d\rho$ for the five different radiation qualities studied in this work. A first glance at the figures shows that the measured and calculated data can be described by a linear function on a double-logarithmic scale. In consequence, $F_1(Q, V)$ is given by a power function in terms of the impact parameter: $F_1(Q, V) = A \times [d\rho/(R\rho)_V]^{-B}$. The results of a least-squares fit of the measured and calculated data with respect to the factor A and the exponent B are presented in figure 11(c) and in table 2 for the five different radiation qualities studied and characterized by $(D\rho)_V/(\lambda\rho)_{\text{ion}}$.

As is obvious from figure 11(c) and table 2, the exponent B of the power function is almost independent of the radiation quality with a mean value of 2.17 for the Monte Carlo data and a mean value of 2.55 for the experimental results. In contrast, the factor A is directly proportional

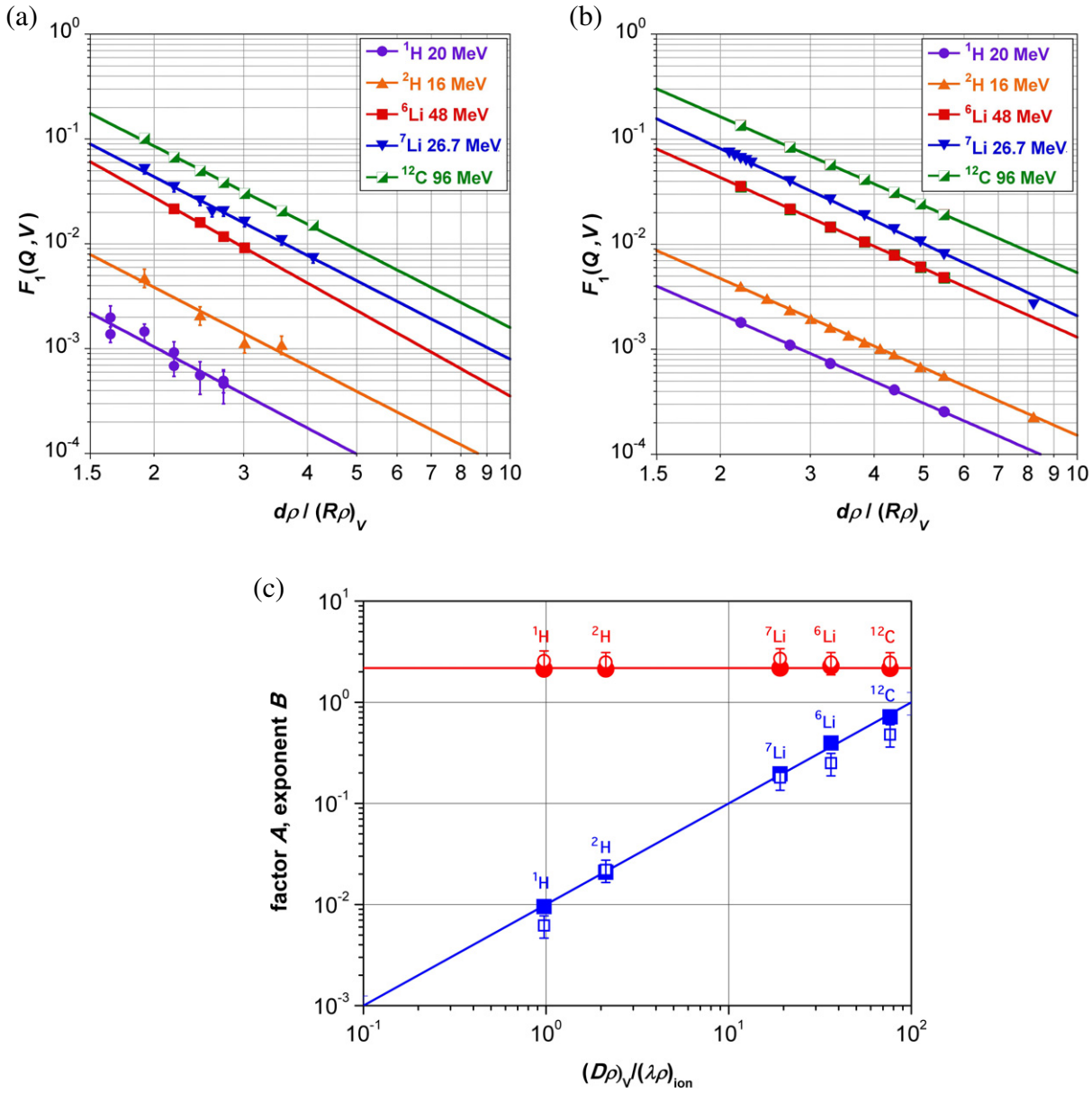

Figure 11. The cumulative distribution function $F_1\,(Q, V)$ as a function of the ratio $d\rho/(R\rho)_V$ of the impact parameter for the penumbra region to the target radius, due to ions at different radiation qualities: (a) measurements, (b) results of the Monte Carlo simulations; symbols, measured or calculated data; unbroken curves, results of a least-squares fit of $F_1(Q,\ V\ ) = A \times \left[d\rho/\ (R\rho)_V\right]^{-B}$ to the data (for the radiation qualities, see the insets). (c) Factor A (squares) and exponent B (circles) presented in table 2, as a function of $(D\rho)_V/(\lambda\rho)_{ion}$. Open symbols correspond to results of the measurements, closed symbols to results of the Monte Carlo simulation.

to the ratio of $(D\rho)_V/(\lambda\rho)_{ion}$ of the diameter of the target volume to the mean free ionization path length of the primary particles, which represents the mean number of δ-electrons set in motion by the primary particles along $(D\rho)_V$. In view of these facts, it can be stated that at

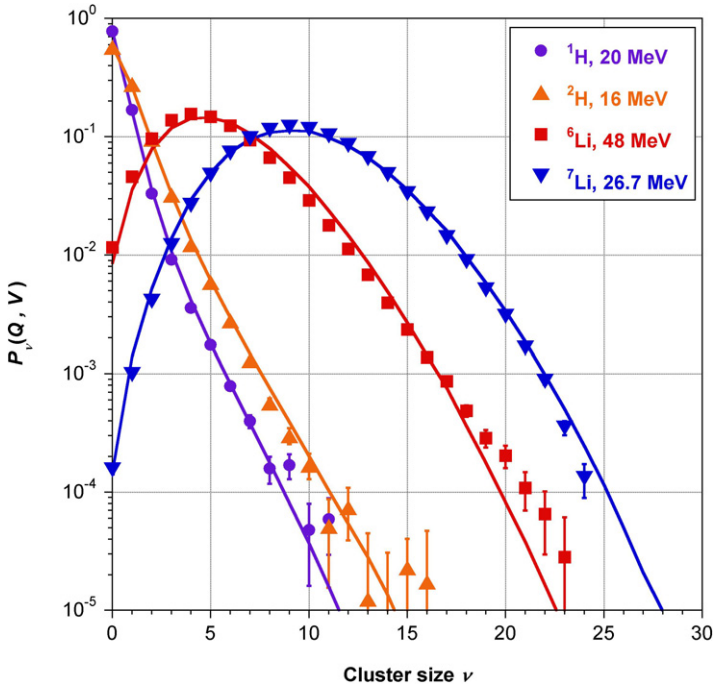

Figure 12. Measured (symbols) and calculated (lines) ionization cluster-size distributions due to 20 MeV protons, 16 MeV deuterons, 48 MeV ^{6}Li-ions and 26.7 MeV ^{7}Li-ions, at impact parameter $d\rho = 0\,\mu g\,cm^{-2}$. Only statistical uncertainties are plotted.

the larger impact parameters studied in this work for the penumbra region the probability of ionization clustering $F_1(Q, V)$ is almost exclusively determined by the number of δ-electrons set in motion by the primary particles.

5.2. Cluster-size distributions

5.2.1. The track-core region. In order to investigate the track structure of particles at a different state of charge Z and velocity, we looked at the ionization cluster-size distributions $P_\nu(Q, V)$, measured and simulated by means of Monte Carlo calculations, at a different impact parameter $d\rho$. To investigate, in particular, the track structure in the so-called 'track-core' region, in figure 12 both experimental and calculated ionization cluster-size distributions $P_\nu(Q, V)$ are shown at impact parameter $d\rho = 0\,\mu g\,cm^{-2}$. The cluster-size distribution due to 20 MeV protons is plotted together with those due to 16 MeV deuterons and 48 MeV ^{6}Li-ions (the two latter particles are moving at approximately the same velocity) and with that due to 26.7 MeV ^{7}Li-ions, which are the ions moving at the lowest velocity, among those examined in this work.

Two different shapes of the cluster-size probability distributions can be clearly observed in this figure: for protons at 20 MeV and for deuterons at 16 MeV, the distributions have high probability at cluster-size equal to zero and values which decrease with increasing cluster size, while the distributions for ^{6}Li-ions at 48 MeV and for ^{7}Li-ions at 26.7 MeV are strongly peaked. The different shapes can be explained by the different ionization densities of the particles. The 20 MeV protons and 16 MeV deuterons have an ionization mean free path length $(\lambda\rho)_{ion}$ of

2.05 and 0.941 μg cm^{-2} respectively, and therefore produce about $(D\rho)_V/(\lambda\rho)_{\text{ion}} = 1$ and 2 ionizations along the volume diameter $(D\rho)_V$, which are reduced to less than 1 if a detector efficiency $\varepsilon = 20\%$ is assumed. In contrast, the ionization density of 26.7 MeV ^{7}Li-ions and 48 MeV ^{6}Li-ions is high enough to produce a peak in the probability distributions.

Generally it can be stated that, for a given Z value, increasing the velocity of the particles causes a shift of the cluster distribution towards a lower cluster-size. This can be observed comparing the distribution for 26.7 MeV ^{7}Li-ions with that for 48 MeV ^{6}Li-ions, which show maxima at around cluster size 9 and 4, respectively. This behaviour is clearly related to the different ionization cross sections and corresponding different values of the particles' ionization mean free path length $(\lambda\rho)_{\text{ion}}$. The 48 MeV ^{6}Li-ions have $(\lambda\rho)_{\text{ion}} = 0.105\,\mu$g cm^{-2} and therefore produce about $(D\rho)_V/(\lambda\rho)_{\text{ion}} = 19$ ionizations along the volume diameter $(D\rho)_V$. If a detector efficiency $\varepsilon = 20\%$ is assumed, a cluster-size of 4 is to be expected. Similarly, the 26.7 MeV ^{7}Li-ions have $(\lambda\rho)_{\text{ion}} = 0.055\,\mu$g cm^{-2} and therefore produce about $(D\rho)_{\text{V}}/(\lambda\rho)_{\text{ion}} =$ 36 ionizations, which are reduced to 7 if a detector efficiency $\varepsilon = 20\%$ is assumed. Both data are in good agreement with the measurements.

It can also be stated that, for a given particle velocity, increasing the Z value causes a shift of the cluster distribution towards higher cluster size, as can be observed comparing the data for 16 MeV deuterons to those relative to 48 MeV ^{6}Li-ions.

The agreement between experimental measurements and the results of Monte Carlo calculations is very satisfactory for all the ions.

5.2.2. The penumbra region. To analyse the differences of track structure in the track-core region and in the penumbra region, figure 13 shows (a) the measured and (b) the calculated distributions due to 26.7 MeV ^{7}Li-ions, at several impact parameters $d\rho$, ranging from $d\rho =$ $0\,\mu$g cm^{-2} up to $d\rho = 2.7\,\mu$g cm^{-2}.

Two different shapes of the cluster-size distributions can be clearly observed in figure 13. In the track-core region, for $d\rho = 0\,\mu$g cm^{-2} and $d\rho = 0.5\,\mu$g cm^{-2}, the primary particles directly cross the volume V and the distributions are both peaked, with a maximum that decreases from about cluster size 9 to about 6, reflecting the shortening of the chord length through V. In the penumbra region, for $d\rho > 1.2\,\mu$g cm^{-2}, ionizations are produced inside V only via δ-electron interactions. Mainly due to the decreasing solid angle, the probability that a δ-ray traverses V also decreases. Consequently, the most probable cluster size is always zero and the probability $P_0(Q, V)$ increases with increasing impact parameter $d\rho$. The shape of the distributions at impact parameters $d\rho \geqslant 1.6\,\mu$g cm^{-2} is similar: $P_\nu(Q, V)$ decreases monotonically with increasing ν, which means that the δ-electrons have a low probability to form large cluster size inside V. At impact parameter $d\rho = 1.1\,\mu$g cm^{-2} the cluster size distribution shows an intermediate shape which is between that for the core region and that for the penumbra region, reflecting the exit of the beam from the volume V.

Measured and calculated distributions are similar in shape, but experimental values for $\nu > 0$ with the beam outside V ($d\rho > 1\,\mu$g cm^{-2}) are systematically lower than corresponding calculated ones. As already observed, this is probably due to a greater number of zero events related to δ-ray electron absorption on ring electrodes, which were not taken into account in the Monte Carlo simulation, or to deficiencies of the applied model (see above).

To further investigate the track-structure characteristics in the penumbra region, figures 14(a) and (b) show the measured and simulated cluster-size distributions due to 48 MeV ^{6}Li-ions at three different impact parameters: $d\rho = 1.6\,\mu$g cm^{-2}, $d\rho = 2.2\,\mu$g cm^{-2} and

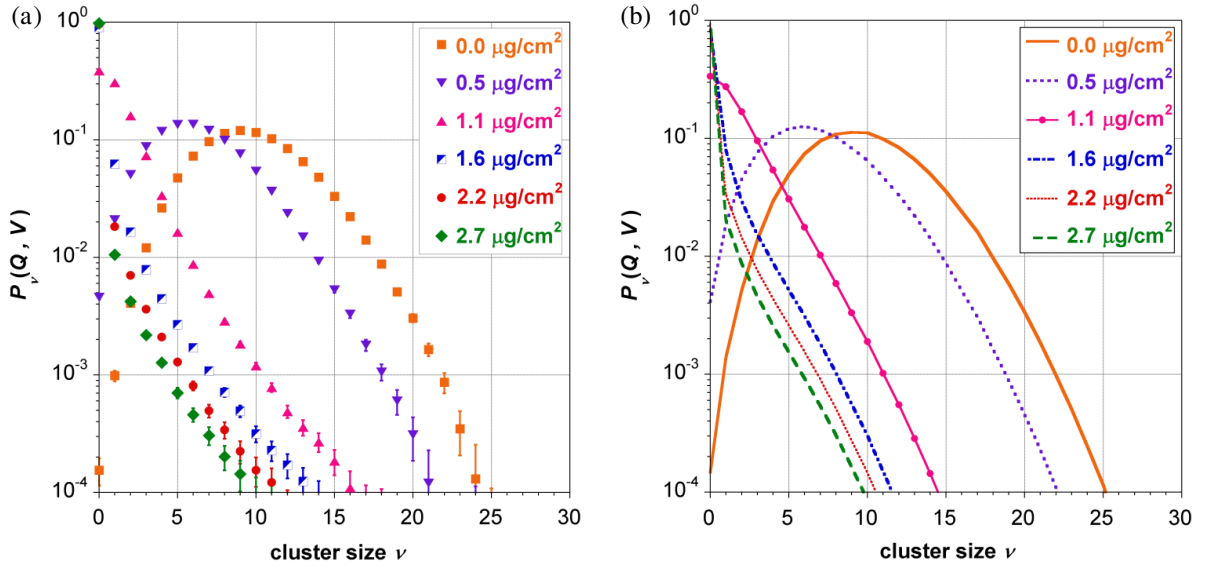

Figure 13. Cluster-size probability distributions due to 26.7 MeV ^{7}Li-ions, at different impact parameter $d\rho$; values of $d\rho$ are specified in the legend: (a) measurements and (b) Monte Carlo simulations. Only statistical uncertainties are plotted.

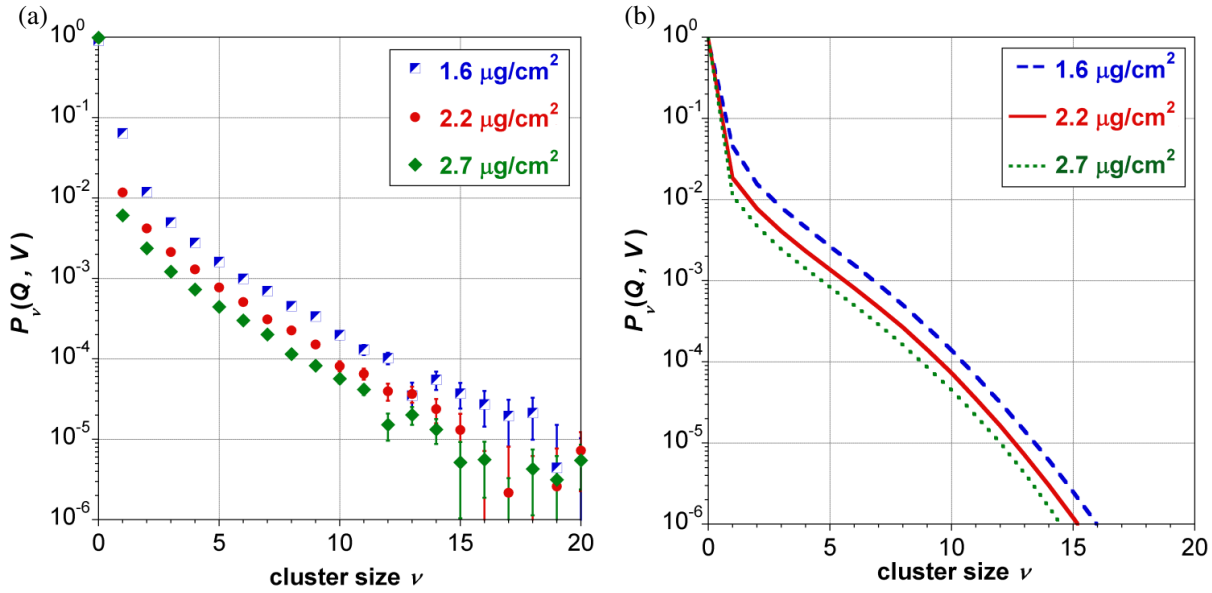

Figure 14. Cluster-size probability distributions due to 48 MeV ^{6}Li-ions at different impact parameters with respect to the primary trajectory: $d\rho = 1.6\,\mu\mathrm{g\,cm^{-2}}$, $d\rho = 2.2\,\mu\mathrm{g\,cm^{-2}}$ and $d\rho = 2.7\,\mu\mathrm{g\,cm^{2}}$; (a) measurements and (b) Monte Carlo calculations. Only statistical uncertainties are plotted.

$d\rho = 2.7\,\mu\mathrm{g\,cm^{-2}}$. In the penumbra region, the three distributions $P_\nu(Q, V)$ have the same shape for $\nu > 0$, independent of impact parameter $d\rho$. They differ only by a constant factor and decrease with increasing impact parameter $d\rho$, mainly due to the decrease of the solid angle,

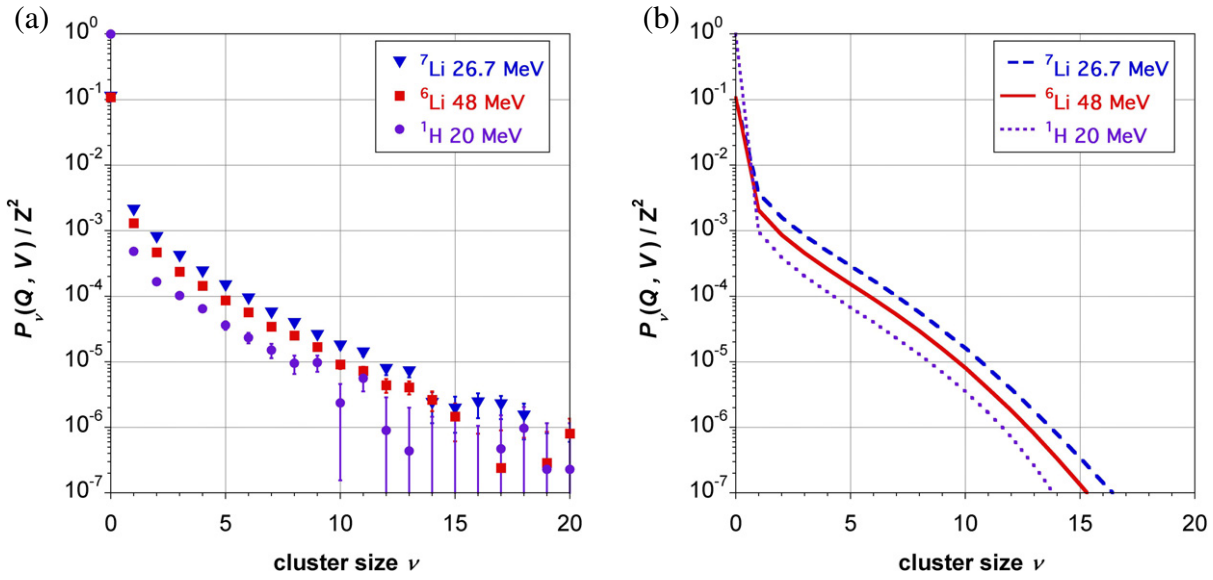

Figure 15. Cluster-size probability distributions due to 26.7 MeV ^{7}Li-ions, 48 MeV ^{6}Li-ions and 20 MeV protons divided by the squared charge state Z^2 of the ions at an impact parameter of $d\rho = 2.2\,\mu\mathrm{g\,cm^{-2}}$: (a) measurements and (b) Monte Carlo calculations. Only statistical uncertainties are plotted.

therefore roughly according to $(d\rho)^{-2}$. Similarly, the cumulative distribution function $F_1(Q, V)$ shows a dependence of impact parameter according to $(d\rho)^{-2.17}$ for the Monte Carlo data and to $(d\rho)^{-2.55}$ for the experimental results, almost independently of radiation quality (see table 2). Similar results on the independence of impact parameter were also found in the measurements with the ion counter by Bashkirov *et al* (2009).

At a specified impact parameter in the penumbra region, it can be assumed that the frequency of cluster-size formation with $\nu > 0$ is mainly determined by the number of δ-electrons set in motion by the primary particles and, in consequence, by the particles' charge state and velocity. For particles at the same velocity but at different charge states, the values of $P_\nu(Q, V)$ for $\nu > 0$ are supposed, therefore, to be proportional to the squared charge state Z^2, and the scaled values $P_\nu(Q, V)/Z^2$ of the cluster-size distributions due to particles at different radiation qualities should be exclusively determined by the particles' velocity. To give an impression of this behaviour of cluster-size distributions in the penumbra region, figure 15 presents the scaled distributions $P_\nu(Q, V)/Z^2$ for $\nu > 0$ due to 26.7 MeV ^{7}Li-ions, 48 MeV ^{6}Li-ions and 20 MeV protons passing the target volume at an impact parameter of $d\rho = 2.2\,\mu\mathrm{g\,cm^{-2}}$.

As expected from the ionization cross section of ionizing particles, which decreases with increasing particle velocity, at least, if the velocity is not too small, the scaled values $P_\nu(Q, V)/Z^2$ of the cluster-size distributions for $\nu > 0$ are smallest for 20 MeV protons; they are greatest for 26.7 MeV ^{7}Li-ions which have a specific energy of 3.81 MeV u^{-1} and thus a markedly smaller velocity than the 20 MeV protons. In consequence, it can be concluded from our measurements and Monte Carlo simulations, that the ionization clustering in the penumbra region is almost exclusively determined by the radiation quality Q of the primary particles, which could be expressed by their mean free ionization path length $(\lambda\rho)_{\mathrm{ion}}$.

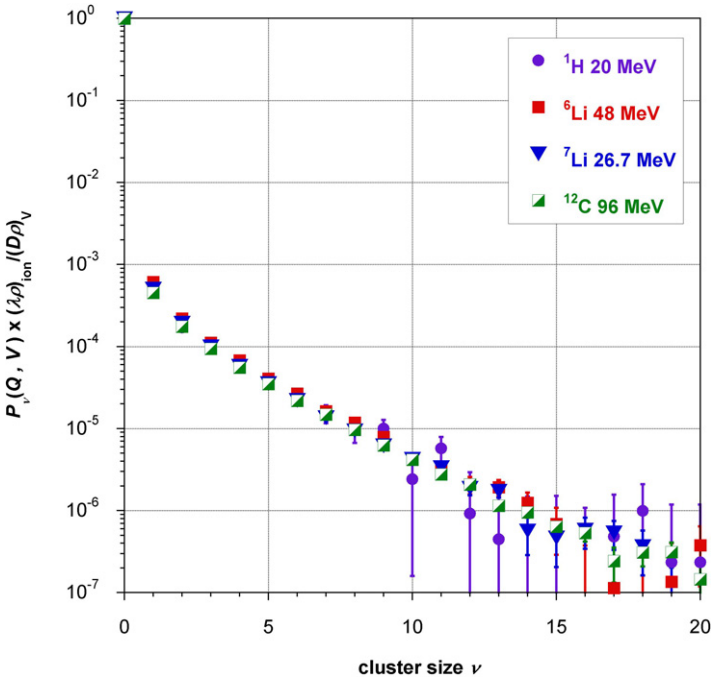

Figure 16. Measured cluster-size distributions due to 20 MeV protons, 26.7 MeV ^{7}Li-ions, 48 MeV ^{6}Li-ions and 96 MeV ^{12}C-ions divided by the ratio $(D\rho)_V/(\lambda\rho)_{\text{ion}}$ of the diameter of the target volume to the mean free ionization path length of the primary particles, at an impact parameter of $d\rho = 2.2\,\mu\text{g cm}^{-2}$. Only statistical uncertainties are plotted.

In order to analyse the influence of radiation quality on the cluster-size distributions caused by ionizing particles in a nanometre-sized target volume V in the penumbra region in greater detail, figure 16 presents the scaled distributions $P_\nu(Q, V) \times (\lambda\rho)_{\text{ion}}/(D\rho)_V$, $\nu = 1, 2, 3, \ldots$, due to 20 MeV protons, 48 MeV ^{6}Li-ions, 26.7 MeV ^{7}Li-ions and 96 MeV ^{12}C-ions passing V at an impact parameter of $d\rho = 2.2\,\mu\text{g cm}^{-2}$. A first glance at the figure immediately shows excellent agreement of the cluster-size distributions for the four different radiation qualities if scaled to the number $(D\rho)_V/(\lambda\rho)_{\text{ion}}$ of δ-electrons set in motion by primary ions along a travelling length $(D\rho)_V$. This excellent agreement of the scaled distributions clearly demonstrates (i) that the shape of the cluster-size distributions at larger impact parameters in the penumbra region are not only independent of impact parameter, as they result from figure 14, but also of radiation quality, and (ii) that the relative cluster-size frequencies for $\nu > 0$ are directly proportional to the number of δ-electrons set in motion by the primary particles.

5.2.3. The conditional cluster-size distribution in the penumbra region. As at relatively large impact parameters $d\rho$ the cluster-size distributions are dominated by zero-sized events, it is interesting to look at the cluster distributions of volumes that have experienced at least one event of ionization, the so-called conditional cluster-size distributions $P^*_\nu(Q, V)$, $\nu = 1, 2, 3, \ldots$,

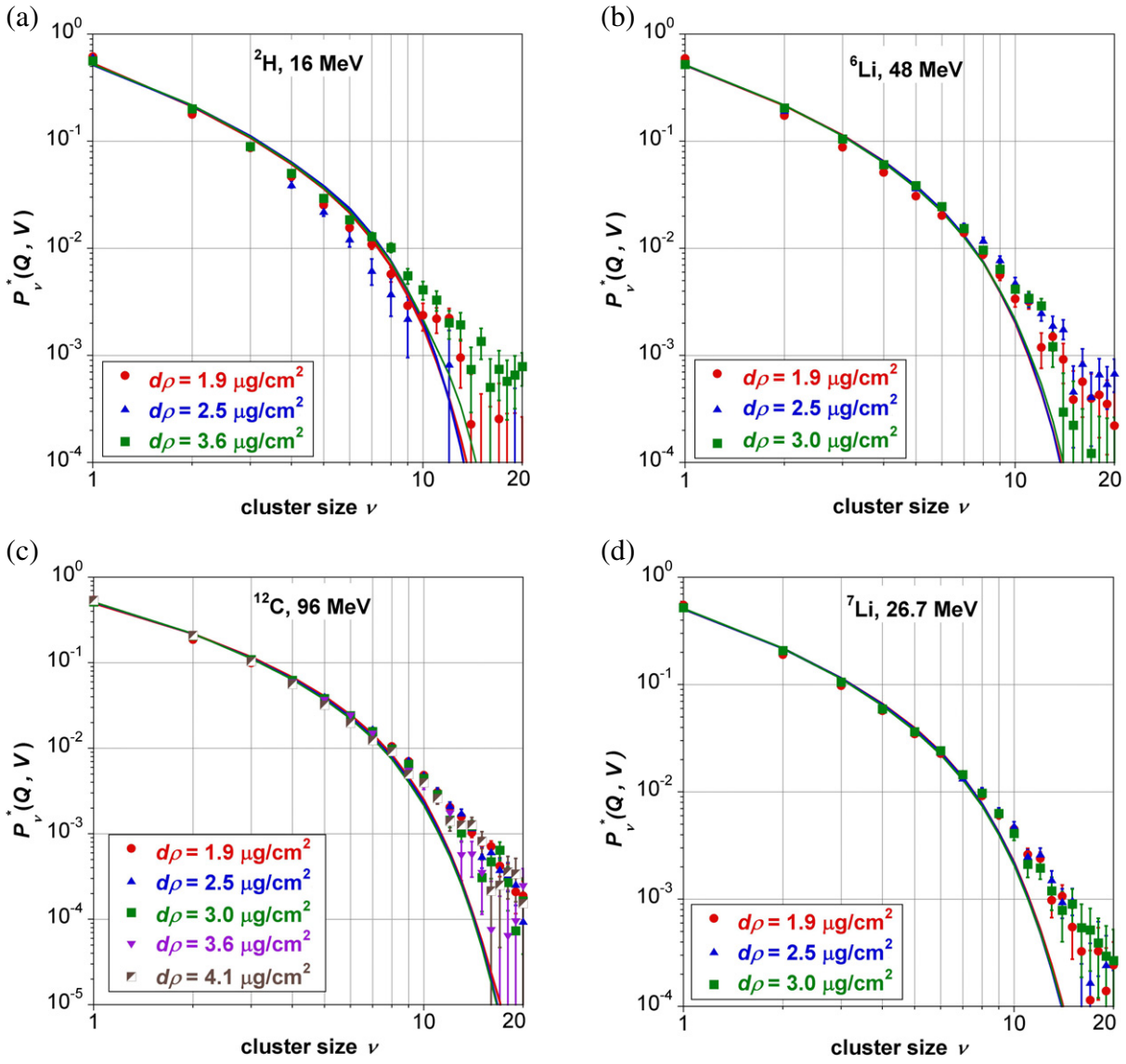

Figure 17. Measured and calculated conditional cluster-size distributions due to: (a) 16 MeV deuterons, (b) 48 MeV ^{6}Li-ions, (c) 96 MeV ^{12}C-ions and (d) 26.7 MeV ^{7}Li-ions, at different impact parameters $dρ$. Only statistical uncertainties are plotted.

which are defined by equation (11).

$$P_ν^*(Q, V) = \frac{P_ν(Q, V)}{F_1(Q, V)}, \quad \text{for } ν \geqslant 1 \quad \text{with} \quad \sum_{ν=1}^{\infty} P_ν^*(Q, V) = 1. \tag{11}$$

Figure 17 shows the measured and simulated conditional cluster-size distributions $P_ν^*(Q, V)$ due to (a) 16 MeV deuterons, (b) 48 MeV ^{6}Li-ions, (c) 96 MeV ^{12}C-ions and (d) 26.7 MeV ^{7}Li-ions at different impact parameters.

After a first glance at the figure it can be observed that for both measurements and simulations the distributions are largely independent of $dρ$, as all the curves overlap almost

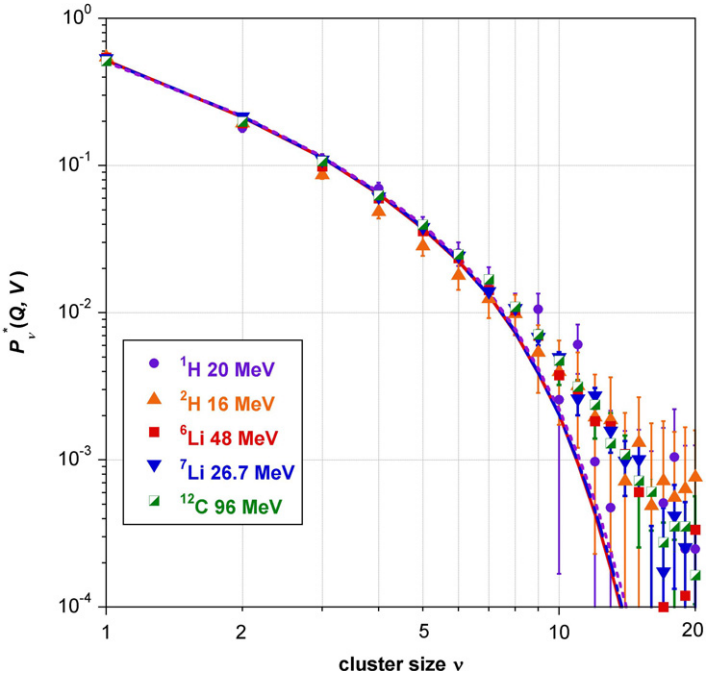

Figure 18. Measured (symbols) and calculated (lines) conditional cluster-size distributions due to 20 MeV protons, 16 MeV deuterons, 48 MeV ^{6}Li and 96 MeV ^{12}C-ions (the last three ions all moving at the same velocity), and to ^{7}Li-ions at an energy of 26.7 MeV. All data refer to a mass impact parameter $d\rho = 2.2\,\mu\mathrm{g\,cm^{-2}}$.

perfectly. Experimental and simulated distributions agree very well at cluster sizes $\nu < 8$ for about two decades, whereas at larger cluster-sizes the experimental distributions are always greater than the simulated ones. To some extent, a similar increase at high clusters was also observed by the ion counting nanodosimeter (see again Bashkirov *et al* (2009)). The reason for this systematic effect could be partly due to an incomplete background subtraction in our measurements, and partly due to deficiencies of the Monte Carlo simulations (see the remarks above). Gas multiplication in the collecting region has to be excluded here, as the electric field strengths are always smaller than $5\,\mathrm{V\,cm^{-1}}$. Secondary electron emission at the electrodes' borders cannot be completely excluded.

To compare distributions due to different radiation qualities, figure 18 represents experimental and calculated conditional cluster-size distributions due to 20 MeV protons, 16 MeV deuterons, 48 MeV ^{6}Li-ions, 96 MeV ^{12}C-ions and 26.7 MeV ^{7}Li-ions at an impact parameter $d\rho = 2.2\,\mu\mathrm{g\,cm^{-2}}$. The conditional cluster-size distributions in the penumbra region are independent of the charge state Z of the primary particle, for a specific energy. This fact was expected, since in the penumbra region the volume V, which is a site of $2\,\mu\mathrm{g\,cm^{-2}}$ in diameter, is mainly traversed by one single δ-ray at a time. Since the secondary electron spectrum is dependent only on the velocity of the primary ion, we expect that only the probability that the target volume is hit changes, while the conditional cluster distribution should be the same. It was, however, less expected that the conditional cluster-size distributions are also largely independent of the velocity of the primary particles, as can be observed by comparing the distributions for 20 MeV protons and 26.7 MeV ^{7}Li-ions.

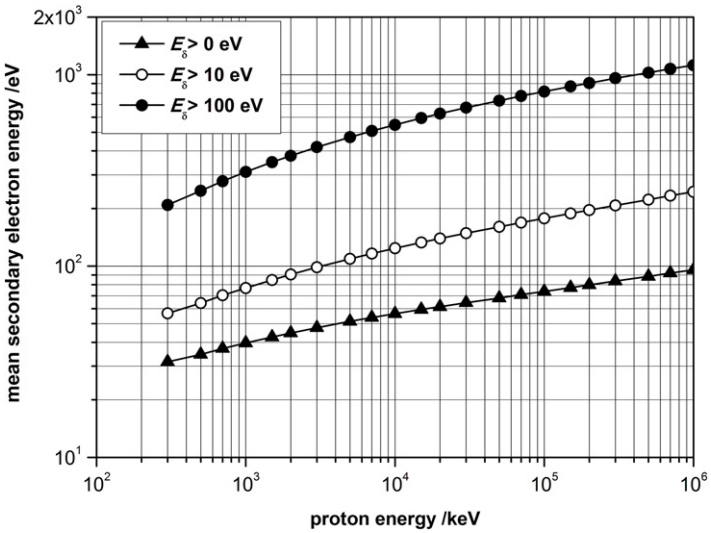

Figure 19. Mean energy of δ-electrons set in motion by protons in propane, as a function of proton energy. Three curves are shown, one (full triangles) with the mean δ-electron energies for all the electrons set in motion by protons, another (empty circles) with the mean δ-electron energies for the electrons set in motion at energies greater than 10 eV and the last one (full circles) for those electrons set in motion at energies greater than 100 eV.

To understand why the conditional distributions are largely independent of the velocity of the primary particles, figure 19 shows the mean energy values of δ-electrons set in motion by protons in propane, as a function of proton energy. Three curves are shown, one (full triangles) with the mean δ-electron energies considering the overall spectrum of all the electrons set in motion by protons, another (empty circles) with the mean δ-electron energies for the electrons set in motion at energies greater than 10 eV and the last one (full circles) for those electrons set in motion at energies greater than 100 eV. In the proton-energy range between 1 MeV and 1 GeV, the mean energy of all δ-electrons set in motion by protons varies only between about 40 and 100 eV, that of δ-electrons with energies greater than 10 eV between about 80 and 250 eV, and that of δ-electrons with energies greater than 100 eV between about 300 eV and 1 keV. It should be noticed that, increasing the proton energy by a factor of 1000, the mean δ-electron energy only increases by a factor of between about 2.5 and 4, for all three populations. This means that the mean δ-electron energy only slightly depends on the energy of the primary particle, as could also be deduced from figure 2, which clearly shows that the shape of the spectral distribution of δ-electrons set in motion in propane by protons at different energies is almost invariant with proton energy.

6. Discussion and conclusions

As discussed extensively by Scholz (2006), the systematic dose response of biological systems to low- and high-LET radiation in dependence on linear energy transfer (LET) or energy can be explained by the properties of particle track structure. Similarly, in his analysis of initial events in the cellular effects of ionizing radiation, Goodhead (1994) formulated a few generalities

that are valid for many biological effects of interest and are also related to the track structure of ionizing particles: (i) cellular responses tend to be stochastic, (ii) the likelihood of residual biological damage at specified absorbed dose increases if the distance between the initial points of particle interactions decreases and (iii) the residual damage from densely ionizing radiation is less open to modifications than that from more sparsely ionizing radiation. These generalities imply that cellular responses are due to some rare events, like the formation of double-strand breaks in DNA molecules, and result, for the greater part, from a clustering of initial damage. The degree of this clustering is responsible for the complexity of the induced damage and is, of course, a result of the particle track structure and of the distance between the target volume and the particle trajectory. As already mentioned in the introduction, it is obvious that the complexity of the damage increases if the distance between successive particle-interaction points decreases, with the result that the ability of cells to recognize and to correctly repair the damaged cluster also decreases.

In view of this importance for radiobiology and health physics, it was the aim of this work to study the track structure of ionizing radiation and, in particular, the ionization clustering caused by ionizing particles in nanometric targets. For this purpose, the ionization-cluster-size formation in a 'nanometre-sized' gaseous volume of propane due to light ions was investigated as a function of the impact parameter, d, defined as the distance between the centre of the target volume and the centre line of narrow beams of the primary ions. The cluster-size formation was studied experimentally using the device based on the single-electron-counting techniques installed at LNL, and numerically by Monte Carlo simulations of the measurements. The measurements and simulations were performed for 16 MeV deuterons, 48 MeV ^{6}Li-ions and 96 MeV ^{12}C-ions, which have the same specific energy of 8 MeV u^{-1} and therefore the same velocity, and, in addition, for 20 MeV protons and 26.7 MeV ^{7}Li-ions. Hence, the radiation qualities of the studied primary ions covered a stopping-power range of between 29.75 MeV cm^2 g^{-1} (20 MeV protons) and 2273 MeV cm^2 g^{-1} (96 MeV ^{12}C-ions), which corresponds to an LET range of between about 3 and 230 keV μm^{-1} at a density of 1 g cm^{-3}.

The target volume of the measuring device had a diameter and a height of 3.7 mm, which corresponds to a mass per area of about 2 μg cm^{-2} at a propane gas pressure of 3 mbar and to a length of 20 nm at a target density of 1 g cm^{-3}. To study the track structure of primary ions in detail and, in particular, the differences of ionization clustering within the core region and the penumbra region of a particle track, the impact parameter was varied between 0 and 8 mm, which corresponds to a mass-per-area range of between 0 and 4.1 μg cm^{-2}, and to distances from 0 to 41 nm at a density of 1 g cm^{-3}.

It should be noticed that the size of the target volume used in this work is markedly smaller than the target volumes used in previous experiments, which ranged from 125 nm to 1.3 μm at a density of 1 g cm^{-3} (Glass and Roesch 1972, Gross and Rodgers 1972, Kliauga and Rossi 1976, Metting *et al* 1988, Toburen *et al* 1990, Schmollack *et al* 2000). These previous experiments were based on the measuring technique developed by Rossi and Rosenzweig (1955) using movable wall-less proportional counters immersed in a large container filled with a tissue-equivalent gas mixture to measure the fluctuation of energy which is absorbed in a target volume due to charged particles penetrating through or passing by. But in view of the stochastics of avalanche formation in proportional counters and of the comparably large target volumes, the stochastics of ionization clustering is hidden in these experiments, at least, for the greater part. In contrast, it can be assumed (i) that the measuring device used in this work is

really able to count single electrons and (ii) that the markedly smaller target volume used in this work leads to ionization-cluster-size distributions that much better reflect the stochastics of ionization clustering if ionizing radiation interacts with the most important radiation sensitive sub-cellular target volumes of living cells (segments of the DNA, nucleosomes and segments of the chromatin fibre).

In this work, the stochastics of ionization clustering are represented by the relative frequency distributions $P_\nu(Q, V)$, $\nu = 0, 1, 2, \ldots$, that exactly a cluster size ν is caused by primary particles of radiation quality Q in a target volume V, the centre of which is separated from the centre line of the primary-particle beam by the impact parameter d. From the point of view of inducing residual biological damage, small cluster sizes represent an ionization clustering with a low complexity of potentially induced initial damage whereas great cluster sizes represent a clustering with induced damage of high complexity which cannot be repaired correctly by a cell (Goodhead 1994).

The analysis of the $P_\nu(Q, V)$-distributions determined in this work could be based on two different data sets, one set determined experimentally and the other by Monte Carlo simulation of the measurements, which are in an excellent agreement for all radiation qualities for the track-core region, and also rather satisfactory for the penumbra region, apart from the larger cluster sizes. Both sets show two different shapes if measured or calculated for impact parameters describing the track-core region or the penumbra region:

(i) one shape with a maximum at a cluster size greater than zero if the distributions represent the properties of the track core, and the primary particles are penetrating through the target volume at a velocity that is not too high and able to produce several ionizations inside V,

(ii) the other shape with a maximum at cluster size zero if the cluster-size formation is exclusively determined by δ-electrons and the distributions represent the penumbra region.

In nanometric target volumes, a primary particle will always exhibit different shapes of the distributions in the two regions, independently of its quality (mass, charge state and velocity). The reason is that in the track-core region the target volume is always traversed by the ionizing particle, whilst in the penumbra-region the volume is hit by a δ-electron only with a low probability. This always leads to a larger fraction of events with cluster size $\nu = 0$ and to a strong drop from $P_0(Q, V)$ to $P_1(Q, V)$. But the two shapes are markedly different only if the average cluster size in the core is >1. If it is <1, the distributions in the track-core region also monotonically decreases from $P_0(Q, V)$, but without the marked drop between $P_0(Q, V)$ and $P_1(Q, V)$ typical of the penumbra region.

As far as the $P_\nu(Q, V)$-distributions for the track-core region are concerned, it can be stated from our measured and calculated data that the cluster size at their maxima increases with the decreasing mean free ionization path length of the primary particles. In consequence, increasing the charge state Z of the primary particles but keeping their velocity constant causes a shift of the cluster-size distribution towards higher cluster sizes. According to the generalities formulated by Goodhead (1994), it can be assumed, therefore, that in this case the likelihood of inducing residual biological damage also increases. In contrast, increasing the particle velocity but keeping their charge state Z constant causes a shift of the cluster-size distribution towards smaller cluster sizes, which should be accompanied by a decrease of the likelihood of inducing residual biological damage.

With respect to the $P_\nu(Q, V)$-distributions for the penumbra region, it can be concluded from the results of this work that the shape of the distributions is on the whole independent of

charge state Z, particle velocity and also of the impact parameter. The absolute values of the $P_\nu(Q, V)$-distributions for $\nu > 0$ decrease with increasing mean free ionization path length of the primary particles due to the decreasing number of δ-electrons, and they differ only by a more or less constant factor. In addition, they decrease to smaller values with increasing impact parameter mainly due to the decreasing solid angle of the target volume seen from the point of setting in motion of δ-electrons due to ionizing interactions of the primary particles. The ratio $P_\nu(Q, V(d_1))/P_\nu(Q, V(d_2))$ of the relative cluster-size frequencies at specified cluster size $\nu > 0$ caused in target volumes at impact parameters d_1 and d_2 by primary particles of radiation quality Q is, therefore, roughly proportional to $(d_2/d_1)^{-2}$, at least, for impact parameters markedly larger than the radius of the target volume. This finding was also confirmed by ionization-chamber experiments (Ohno *et al* 1997), and supports the common assumption of amorphous track-structure models (see, for instance, Cucinotta *et al* (1999)) and also of the local effects model (Scholz and Kraft 1994, Scholz *et al* 1997) that the radial dose varies essentially with $1/d^2$.

To get rid of the $1/d^2$-dependence of the $P_\nu(Q, V)$-distributions for $\nu > 0$, and to study the properties of ionization clustering in the penumbra region in greater detail, the conditional cluster-size distributions $P^*_\nu(Q, V)$, $\nu = 1, 2, 3, \ldots$, were also analysed. These distributions represent the stochastics of cluster-size formation provided that at least one ionizing event of a particle track is included in the target volume. After the analysis of the measured and calculated conditional distributions it can be stated that

(i) the shape of the $P^*_\nu(Q, V)$-distributions in the penumbra region due to primary particles at specified radiation quality Q is largely independent of the impact parameter,

(ii) the $P^*_\nu(Q, V)$-distributions in the penumbra region are not only independent of the charge state Z of the primary particles but also of their velocity.

These findings concerning the 'general behaviour' of the cluster-size distributions in the penumbra region are independent of the detector efficiency. They can be explained by the fact that in nanometre-sized target volumes at larger impact parameters the cluster-size distributions are due to single δ-electrons the energies of which do not strongly depend on the average of the primary particles' velocity. Similar results were also obtained for much larger target volumes in the proportional-counter experiments mentioned above, for smaller target volumes by Bashkirov *et al* (2009), and in previous Monte Carlo simulations concerning the frequency of energy deposition events produced in small sites by high-energy δ-electrons (Kellerer and Chmelevsky 1975, Wilson *et al* 1988, Wilson 1994, Wilson and Paretzke 1994, Wang *et al* 2006). The results of these simulations show that, although the energy distribution of δ-electrons set in motion by primary particles depends on their velocity, the energy deposited by δ-electrons in small sites is relatively independent of the particles' velocity and of the impact parameter.

In summary, it can be stated that the distributions determined for a target volume with a diameter of $2\,\mu\mathrm{g\,cm^{-2}}$ in mass per area as a function of the impact parameter show similar behaviour to that expected for the dose response of biological systems (Scholz 2006) if interpreted in terms of the generalities formulated by Goodhead (1994) with respect to the explanation of the initial events in the cellular effects of ionizing radiation in terms of damage clustering. This is obvious if the values of the cumulative distribution function $F_1(Q, V)$ presented in figure 10 are analysed in terms of the ratio $(D\rho)_V/(\lambda\rho)_{\mathrm{ion}}$ of the diameter of the target volume to the mean free ionization path length of the primary particles with the impact parameter $d\rho$ as a parameter. In figure 20(a), $F_1(Q, V)$ is given for the track-core region at

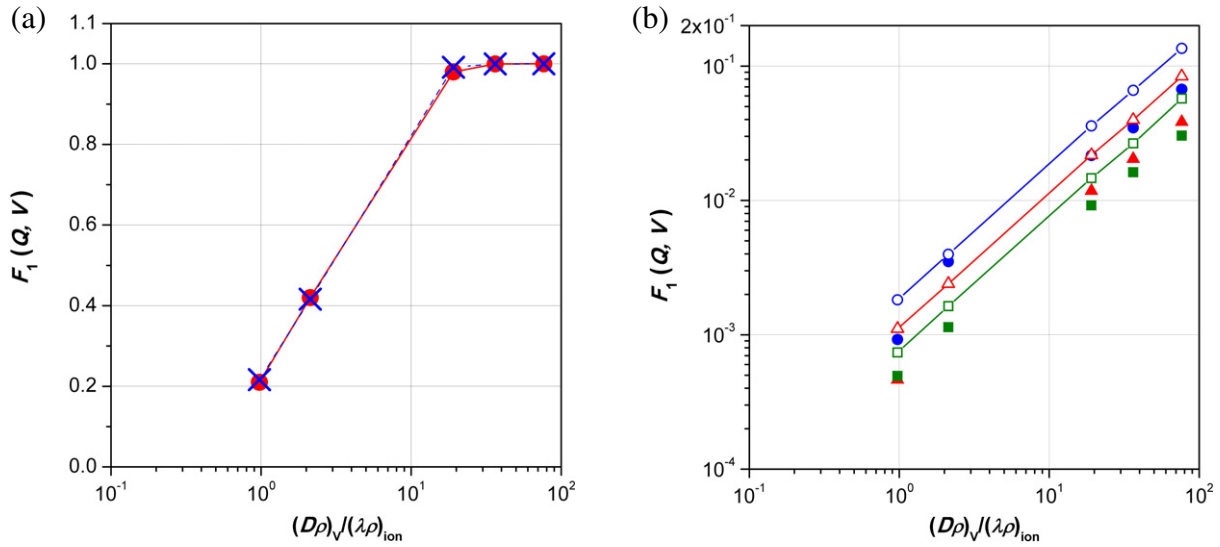

Figure 20. Relative frequency of ionization clustering $F_1(Q, V)$ as a function of the ratio $(D\rho)_V/(\lambda\rho)_{ion}$ of the diameter of the target volume to the mean free ionization path length of the primary particles: (a) measured (•) and calculated values (×) at $d\rho = 0\,\mu g\,cm^{-2}$, (b) measured and calculated values in the penumbra region: (○, •) $d\rho = 2.2\,\mu g\,cm^{-2}$, (△, ▲) $d\rho = 2.7\,\mu g\,cm^{-2}$, (□) $d\rho = 3.2\,\mu g\,cm^{-2}$ and (■) $d\rho = 3.0\,\mu g\,cm^{-2}$; open symbols, results of Monte Carlo simulation; closed symbols, results of measurements.

$d\rho = 0\,\mu g\,cm^{-2}$, and in figure 20(b) it is given for the penumbra region, at four different impact parameters. It can be easily seen in figure 20(a) that the probability of ionization clustering strongly increases in the track-core region with increasing values of $(D\rho)_V/(\lambda\rho)_{ion}$ and reaches saturation for large values of $(D\rho)_V/(\lambda\rho)_{ion}$. We believe that this saturation is related to the saturation effect of radiobiological cross sections for high-LET radiation and to the decrease of the relative biological effectiveness with increasing LET in the high-LET range (Scholz 2006). With decreasing $(D\rho)_V/(\lambda\rho)_{ion}$, $F_1(Q, V)$ also decreases with the result of decreasing damage complexity and, therefore, also decreasing likelihood of residual biological damage. In the penumbra region (see figure 20(b)), $F_1(Q, V)$ is much smaller than that for the track-core region, and it decreases with decreasing $(D\rho)_V/(\lambda\rho)_{ion}$, demonstrating a decrease of the probability of ionization clustering and, therefore, also a decrease of the likelihood of residual damage.

The geometry of this experiment allows for measurements at specified impact parameters, whilst the geometry leading to complexity of radiation damage in a homogeneous field is completely different. Biological effects typically average over the whole distribution of traversing primary particle and δ-electron trajectories. In spite of this, we believe that the data presented in figure 20(a) are meaningful for representing the efficiency of radiation to induce radiobiological damage. As far as the average over different trajectories is concerned, it should be noticed that $F_1(Q, V)$ represents the probability that at least one ionization is produced inside the target volume and, for crossing particles, it strongly depends on the ratio $(L\rho)_V/(\lambda\rho)_{ion}$ of the path length $(L\rho)_V$ of the particle inside the target volume to the mean free ionization path length $(\lambda\rho)_{ion}$ of the primary particle. In consequence, when measured

along a different crossing trajectory and plotted as a function of $(L\rho)_V/(\lambda\rho)_{\mathrm{ion}}$, the $F_1(Q, V)$ value lies approximately on the same curve shown in figure 20(a), almost independently of impact parameter, in the track-core region. On the other side, in the penumbra region, the contribution of a single δ-electron to the total $F_1(Q, V)$ is always negligible, as compared to that of primary particles, due to the large fraction of zero events (see for example figure 16). In order to directly relate our measurements at specified impact parameters to radiobiological measurements, the track-structure data should be integrated according to the applied radiation field. This procedure, and the possible implications of its results, needs to be further investigated.

Summarizing, we measured cluster-size distributions in a 20 nm-sized site, with an overall detection efficiency of about 20%. It is clear that a different site size, or a different efficiency, would lead to different shapes of measured cluster-size distributions. To what extent the properties of track-structure measurements in 20 nm-sized sites are significant to describe the effectiveness of different radiations to induce radiobiological damage, is a matter for future investigations. On the other hand, our measurements validate the used Monte Carlo simulation code (see also De Nardo *et al* (2002a) and Garty *et al* (2002a)), which in its core part has also been validated by the independent track-structure measurements performed in propane gas with positive ion-counting techniques (Bashkirov *et al* 2009). Therefore, the code can be used confidently to investigate the track structure of charged particles in propane volumes of different sizes at arbitrary detection efficiencies. The results of Monte Carlo simulations in nanometric cylindrical volumes at 100% efficiency will be presented and discussed in a future paper.

Further effort should be invested in the future to relate ionization-cluster-size distributions measured for primary particles in a broad LET range to the results of radiobiological experiments in order to define track-structure based descriptors of radiation quality that are measurable and behave as a function of radiation quality similar to specified radiation-induced biological effects. As far as the relation between radiation physics and radiobiology is concerned, the cluster-size formation in the track-core and the penumbra region should also be measured using target volumes comparable in size with nucleosomes and, in particular, with short segments of the DNA that are assumed today to be the most important radiation-sensitive biological target volumes with respect to radiation-induced damage to genes and cells. The relation of radiobiological data and parameters derived from ionization cluster-size distributions is extensively illustrated and discussed in several papers (see, for instance, Grosswendt 2004, 2005, 2006, 2007, Garty *et al* 2006, 2010, Grosswendt *et al* 2007, Schulte *et al* 2008, Bantsar *et al* 2009). In particular, Garty *et al* and Schulte *et al* described and applied a complete nanodosimetric model of radiation-induced DNA damage, based on a combinatorial approach to translate ionizations caused by ionizing particles in gas volumes to lesions in short DNA segments.

From the point of view of radiation protection, and of treatment planning and quality assurance for purposes of radiation therapy, the development is urgently needed of practical instruments that are able to measure the properties of particle track structure but can be used easily in unknown fields, or in hospitals to measure radiation quality. Our apparatus can image the track structure of different ions with 20 nm resolution, but it is not by far a practical instrument, because of its large size and complexity of operation. The development of miniaturized microdosimeters with 'nanometre'-sized sensitive volumes could be of interest to bridge the gap between traditional experimental microdosimetry, nanodosimetry and particle track structure.

Acknowledgments

This work is supported by the 5th scientific commission of the Istituto Nazionale di Fisica Nucleare of Italy. We thank Marco Poggi, Davide Carlucci and the whole XTU-Tandem accelerator staff for their technical assistance during the accelerator operations, always provided with competence and generosity.

References

Amaldi U and Kraft G 2007 European developments in radiotherapy with beams of large radiobiological effectiveness *J. Radiat. Res.* (*Suppl.* A) **48** A27–41

Bantsar A, Grosswendt B, Kula J and Pszona S 2004 Clusters of ionisation in nanometre targets for propane-experiments with a jet counter *Radiat. Prot. Dosim.* **110** 845–50

Bantsar A, Grosswendt B, Pszona S and Kula J 2009 Single track nanodosimetry of low energy electrons *Nucl. Instrum. Methods Phys. Res.* A **599** 270–4

Bashkirov V, Schulte R, Breskin A, Chechik R, Garty G, Wroe A and Grosswendt B 2006 Ion-counting nanodosimeter with particle tracking capabilities *Radiat. Prot. Dosim.* **122** 415–9

Bashkirov V, Schulte R, Wroe A, Sadrozinski H, Gargioni E and Grosswendt B 2009 Experimental validation of track structure models *IEEE Trans. Nucl. Sci.* **56** 2859–63

Chu W T T 2007 Overview of light-ion beam therapy *Dose Reporting in Ion Beam Therapy* IAEATECDOC-1560 (Vienna: IAEA) pp 5–28

Cole A 1969 Absorption of 20 eV to 50 000 eV electron beams in air and plastic *Radiat. Res.* **38** 7–33

Conte V, Colautti P, De Nardo L, Ferretti A, Poggi M, Moro D, Lombardi M, Tornielli G and Grosswendt B 2011 Track nanodosimetry of 20 MeV protons at 20 nm *Radiat. Prot. Dosim.* **143** 455–8

Conte V, De Nardo L, Colautti P, Ferretti A, Grosswendt B, Lombardi M, Poggi M, Canella S, Moro D and Tornielli G 2010 First track-structure measurements of 20 MeV protons with the STARTRACK apparatus *Radiat. Meas.* **45** 1213–6

Cucinotta F A and Durante M 2006 Cancer risk from exposure to galactic cosmic rays: implications for space exploration by human beings *Lancet Oncol.* **7** 431–5

Cucinotta F A, Nikjoo H and Goodhead D T 1999 Applications of amorphous track models in radiation biology *Radiat. Environ. Biophys.* **38** 81–92

De Nardo L, Alkaa A, Khamphan C, Conte V, Colautti P, Ségur P and Tornielli G 2002b A detector for track-nanodosimetry *Nucl. Instrum. Methods Phys. Res.* A **484** 312–6

De Nardo L, Colautti P, Conte V, Baek W Y, Grosswendt B and Tornielli G 2002a Ionization-cluster distributions of α-particles in nanometric volumes of propane: measurement and calculation *Radiat. Environ. Biophys.* **41** 235–56

De Nardo L, Colautti P and Grosswendt B 2006 Simulation of the measured ionisation-cluster distributions of alpha-particles in nanometric volumes of propane *Radiat. Prot. Dosim.* **122** 427–31

De Nardo L, Conte V, Poggi M, Canella S, Colautti P, Moro D and Tornielli G 2007 The STARTRACK experiment *Radiat. Prot. Dosim.* **126** 453–6

Elsässer T, Cunrath R, Krämer M and Scholz M 2008 Impact of track structure calculations on biological treatment planning in ion radiotherapy *New J. Phys.* **10** 075005

ESTAR Stopping Powers and Ranges for Electrons http://physics.nist.gov/PhysRefData/Star/Text/method.html

Gargioni E and Grosswendt B 2007 Influence of ionization cross-section data on the Monte Carlo calculation of nanodosimetric quantities *Nucl. Instrum. Methods Phys. Res.* A **580** 81–4

Garty G, Schulte R, Shchemelinin S, Grosswendt B, Leloup L, Assaf G, Breskin A, Chechik R and Bashkirov V 2006 First attempts at prediction of DNA strand-break yields using nanodosimetric data *Radiat. Prot. Dosim.* **122** 451–4

Garty G, Schulte R, Shchemelinin S, Leloup C, Assaf G, Breskin A, Chechik R, Bashkirov V, Milligan J and Grosswendt B 2010 A nanodosimetric model of radiation-induced clustered DNA damage yields *Phys. Med. Biol.* **55** 761–81

Garty G, Shchemelinin S, Breskin A., Chechik R, Assaf G, Orion I, Bashkirov V, Schulte R and Grosswendt B 2002a The performance of a novel ion-counting nanodosimeter *Nucl. Instrum. Methods Phys. Res.* A **492** 212–35

Garty G, Shchemelinin S, Breskin A, Chechik R, Orion I, Guedes G P, Schulte R, Bashkirov V and Grosswendt B 2002b Wall-less ion-counting nanodosimetry applied to protons *Radiat. Prot. Dosim.* **99** 325–30

Glass W A and Roesch W C 1972 Measurement of ionisation distributions in tissue-equivalent gas *Radiat. Res.* **49** 477–94

Goodhead D T 1994 Initial events in the cellular effects of ionizing radiations: clustered damage in DNA *Int. J. Radiat. Biol.* **65** 7–17

Gross W and Rodgers R C 1972 Heavy Ion event spectra *Proc. 3rd Symp. on Microdosimetry* EUR 4810 d-e-f CEC Luxembourg 873–85

Grosswendt B 2004 Recent advances of nanodosimetry *Radiat. Prot. Dosim.* **110** 789–99

Grosswendt B 2005 Nanodosimetry, from radiation physics to radiation biology *Radiat. Prot. Dosim.* **115** 1–9

Grosswendt B 2006 Nanodosimetry, the metrological tool for connecting radiation physics with radiation biology *Radiat. Prot. Dosim.* **122** 404–14

Grosswendt B 2007 From macro to nanodosimetry: limits of the absorbed-dose concept and definition of new quantities *Proc. Int. Workshop on Uncertainty Assessment in Computational Dosimetry (Bologna, 8–10 October 2007)* ed G Gualdrini and P Ferrari (Bologna: ENEA)

Grosswendt B, De Nardo L, Colautti P, Pszona S, Conte V and Tornielli G 2004 Experimental equivalent cluster-size distributions in nanometric volumes of liquid water *Radiat. Prot. Dosim.* **110** 851–7

Grosswendt B, Pszona S and Bantsar A 2007 New descriptors of radiation quality based on nanodosimetry, a first approach *Radiat. Prot. Dosim.* **126** 432–44

Hilgers G, Gargioni E, Grosswendt B and Shchemelinin S 2007 Proton-induced frequency distributions of ionization cluster size in propane *Radiat. Prot. Dosim.* **126** 467–70

Hwang W, Kim Y-K and Rudd M E 1996 New model for electron-impact ionization cross sections of molecules *J. Chem. Phys.* **104** 2956–66

ICRU 1979 Average energy required to produce an ion pair *Report 31, International Commission on Radiation Units and Measurements* (Washington, DC: ICRU)

ICRU 1996 Secondary electron spectra from charged particle interactions *Report 55, International Commission on Radiation Units and Measurements* (Bethesda, MD: ICRU)

Kase Y, Kanai T, Matsufuji N, Furusawa Y, Elsässer T and Scholz M 2008 Biophysical calculation of cell survival probabilities using amorphous track structure models for heavy-ion irradiation *Phys. Med. Biol.* **53** 37–59

Kellerer A M and Chmelevsky D 1975 Concepts of microdosimetry III. mean values of the microdosimetric distributions *Radiat. Environ. Biophys.* **12** 321–35

Kliauga P and Rossi H H 1976 Microdosimetric distributions as a function of radial distance from heavy ion tracks *Proc. 5th Symp. on Microdosimetry* EUR 5452 d-e-f CEC Luxembourg, pp 127–40

Metting N F, Rossi H H, Braby L A, Kliauga P J, Howard J, Zaider M, Schimmerling W, Wong M and Rapkin M 1988 Microdosimetry near the trajectory of high-energy heavy ions *Radiat. Res.* **116** 183–95

Ohno S, Furukawa K, Taguchi M, Namba H and Watanabe R 1997 A track structure model based on measurements of radial dose distribution around an energetic heavy ion *Microdosimetry: An Interdisciplinary Approach* ed D T Goodhead *et al* (Cambridge: Royal Society of Chemistry) pp 31–4

Pszona A, Kula J and Marjanska S 2000 A new method for measuring ion clusters produced by charged particles in nanometre track sections of DNA size *Nucl. Instrum. Methods Phys. Res.* A **447** 601–7

Rossi H H and Rosenzweig W 1955 A device for the measurement of dose as a function of specific ionization *Radiology* **64** 404–11

Schmollack J U, Klaumuenzer S L and Kiefer J 2000 Stochastic radial dose distributions and track structure theory *Radiat. Res.* **153** 469–78

Scholz M 2006 Dose response of biological systems to low- and high-LET radiation *Microdosimetric Response of Physical and Biological Systems to Low- and High-LET Radiations: Theory and Applications to Dosimetry* ed Y Horowitz (Amsterdam: Elsevier) pp 1–73

Scholz M and Kraft G 1994 Calculation of heavy ion inactivation probabilities based on track structure, x-ray sensitivity and target size *Radiat. Prot. Dosim.* **52** 29–33

Scholz M, Kellerer A M, Kraft-Weyrather W and Kraft G 1997 Computation of cell survival in heavy ion beams for therapy. The model and its approximation *Radiat. Environ. Biophys.* **36** 59–66

Schulte R W 2011 Nanodosimetry: principle and current status *AIP Conf. Proc.* **1345** 249–61

Schulte R W, Wroe A J, Bashkirov V B, Garty G Y, Breskin A, Chechik R, Shchemelinin S, Gargioni E, Grosswendt B and Rosenfeld A 2008 Nanodosimetry-based quality factors for radiation protection in space *Z. Med. Phys.* **18** 286–96

Shchemelinin S, Garty G, Breskin A, Chechik R and Schulte R W M 2002 Ion-counting nanodosimetry: a new method for assessing radiation damage to DNA *Nucl. Instrum. Methods Phys. Res.* A **477** 527

Toburen L H, Braby L A, Metting N F, Kraft G, Scholz M, Kraske F, Schmidt-Böcking H, Dörner R and Seip R 1990 Radial distributions of energy deposited along charged particle tracks *Radiat. Prot. Dosim.* **31** 199–203

Wambersie A, Henry J H, Andreo P, DeLuca P M, Gahbauer R, Menzel H and Whitmore G 2006 The RBE issues in ion-beam therapy: conclusions of a joint IAEA/ICRU working group regarding quantities and units *Radiat. Prot. Dosim.* **122** 463–70

Wang X, Liu H, Xia Z and Braby L A 2006 Lineal energy as a function of site size for HZE radiation *Radiat. Prot. Dosim.* **122** 367–8

Wilson W E 1994 The stochastic of the positive ion penumbra *Radiat. Res.* **140** 375–81

Wilson W E and Paretzke H G 1994 A stochastic model of ion track structure *Radiat. Prot. Dosim.* **52** 249–53

Wilson W E, Metting N F and Paretzke H G 1988 Microdosimetric aspects of 0.3 to 20 MeV proton tracks. *Radiat. Res.* **115** 389–402

Wroe A J, Schulte R, Bashkirov V, Rosenfeld A B, Keeney B, Spradlin P, Sadrozinski H F W and Grosswendt B 2006 Nanodosimetric cluster size distributions of therapeutic proton beams *IEEE Trans. Nucl. Sci.* **53** 532–8